©2018

Arielle J. Catalano

ALL RIGHTS RESERVED

STORM SURGE-PRODUCING EXTRATROPICAL CYLONES IN THE NORTHEASTERN UNITED STATES IN OBSERVATIONS AND MODELS

By

ARIELLE J. CATALANO

A dissertation submitted to the

School of Graduate Studies

Rutgers, The State University of New Jersey

In partial fulfillment of the requirement

For the degree of

Doctor of Philosophy

Graduate Program in Atmospheric Science

Written under the direction of

Anthony J. Broccoli

And approved by

_____

_____

_____

_____

New Brunswick, New Jersey

October, 2018

ABSTRACT OF THE DISSERTATION

Storm Surge-Producing Extratropical Cyclones in the Northeastern United States in Observations and Models

By

ARIELLE J. CATALANO

Dissertation Director:

Anthony J. Broccoli

In the northeastern United States, extratropical cyclones (ETCs) are associated with the majority of the largest storm surges, which significantly impact coastal regions. We characterize the synoptic evolution of the largest ETC-driven surge events in observations and a long record from a coupled climate model representing recent climate conditions. A *k*-means cluster analysis is applied to the top 100 observed surge-producing ETCs at select locations (Sewells Point, Virginia; The Battery, New York; and Boston, Massachusetts) to group similar circulation features. These distinct patterns suggest that the largest surges are generated when slowly propagating ETCs encounter a strong anticyclone, which produces a tighter pressure gradient and longer duration of onshore winds. Multiple clusters feature a slower-than-average storm and a strong anticyclone, indicating that various circulation scenarios with these features can produce a large surge. This favorable environment is influenced by El Niño conditions, and maximum surge

occurs preferentially during the positive phase of PNA and the negative phases of AO/NAO.

Return periods of the largest ETC-driven surge events are difficult to estimate owing to the short duration of high-quality observational datasets, so a long simulation from a coupled model, GFDL FLOR, is employed. Distributions of meteorological quantities that influence surge height (i.e. central pressure and surface winds) indicate that the longer integration contains a greater number of extreme ETCs. An exceedance probability risk assessment of the strongest impacts demonstrates a consistent underestimation in historical-length records compared to return levels estimated from the full FLOR simulation. This indicates that if the underlying distributions of observed metrics are similar to those of the 1505-year record, the actual frequency of extreme events is being underestimated.

Comparisons of cyclone statistics between FLOR and a reanalysis product, CFSR, exhibit biases in quantitative measures of storm surge and intensity, but characteristics of the distributions of these quantities are representative of features of a climate constrained by observations. A *k*-means cluster analysis of the synoptic evolution of storm surge events estimated using a regression-based index displays similar circulation features to clusters of observed events. At The Battery and Sewells Point, clusters containing the majority of the largest estimated storm surges exhibit a strong anticyclone and a slow-moving cyclone. Discrepancies at Boston are related to approximations made by the regression index applied to identify and arrange clustered meteorological patterns.

ACKNOWLEDGEMENTS

This work would not be possible without the incredible insight, guidance, and patience of my advisor, Dr. Tony Broccoli. As a mentor, both professionally and personally, Dr. Broccoli has helped me develop into a successful scientist. It has truly been an honor to work with him these past few years.

I also thank the other members of my dissertation committee. Dr. Sarah Kapnick has been an exceptional role model, providing encouragement and advice throughout my dissertation. Dr. Steven Decker's vast knowledge of meteorology has been a valuable contribution to this work. Dr. Benjamin Lintner was always available to answer questions, and he continually notified me of opportunities that would advance my career, for which I am grateful.

Thank you to Bryan Raney, Marjorie Kaplan, Melissa Arnesen, and all Department of Environmental Sciences faculty and staff for their guidance, service, and warmth that made Rutgers a wonderful place to work.

To Dr. Caroline Farkas, Dr. Khoi Nguyen, Jenny Kafka, Max Pike, Matt Drews, and many other past and present graduate students – your friendship and support were fundamental to my success.

My husband, family, and friends have been my fiercest cheerleaders. Thank you for the advice and love that have helped me withstand the ups and downs of graduate school to accomplish this high school ambition.

Financial support for this research was generously provided by the William H. Greenberg Fellowship from Rutgers University and the National Science Foundation

Earth System Modeling Program (OCE1049088). Part of this work was published in the Journal of Applied Meteorology and Climatology, titled “Synoptic Characteristics of Surge-Producing Extratropical Cyclones along the Northeast Coast of the United States” by Arielle J. Catalano and Anthony J. Broccoli, for which the American Meteorological Society holds copyright.

TABLE OF CONTENTS

LIST OF TABLES

LIST OF ILLUSTRATIONS

CHAPTER 1

Introduction and Review of Literature

1.1. Motivation

Severe coastal storms devastate communities around the world with significant socioeconomic impacts in densely populated areas. These storms possess strong winds and heavy precipitation, which cause widespread flooding, property damage, and loss of life. Increasing resilience of coastal communities and mitigating flood risks are ongoing efforts. The North Atlantic Coast Comprehensive Study established a tiered management framework for vulnerable communities, which includes collaboration among shareholders, governing entities, and the public (USACE 2015). Continued research informs these decision-making processes by increasing our understanding of coastal risks since uncertainty remains. In October 2012, Hurricane Sandy caused an estimated $65 billion in damages and losses, driving research to examine exposure to severe and devastating impacts including inundation. Previous work has assessed flood risk (e.g. Lin et al. 2010; Lin et al. 2012; Reed et al. 2015; Orton et al. 2016) and storm track variability (Booth et al. 2015; Booth et al. 2016), which affects the frequency of coastal impacts. However, few studies have investigated the physical mechanisms of inundation events such as atmospheric circulation features.

Although Hurricane Sandy generated the largest storm surge (and storm tide) in recorded history at multiple tide gauges in the northeastern United States, the majority of large

surge events in this region are associated with extratropical cyclones (ETCs) rather than tropical systems. Storm surge is measured as the difference between the overall water level and the astronomical tide, assuming nonlinear interactions are insignificant (Zhang et al. 2000). ETCs have generated 88 of the top 100 storm surge events at The Battery in New York City, and 91 of the 100 largest at Boston, Massachusetts (Table 1.1). Some of the most damaging surge-producing ETCs exhibit low central pressures or exceptionally strong low-level winds, the duration and direction of which drive ocean water inland (Bernhardt and DeGaetano 2012). For example, the Storm of the Century in March 1993 experienced explosive cyclogenesis and deepened rapidly at a rate of over 1 hPa per hour at an unusually low latitude (Kocin et al. 1995). This storm was associated with the sixth largest ETC-driven storm surge recorded at The Battery, New York (1920–2010) and the eleventh largest at Boston, Massachusetts (1921–2010), with wind gusts exceeding hurricane force at Boston and Fire Island, NY. Another notable ETC-driven storm surge event was the Great Appalachian Storm of November 1950 (Smith 1950), which produced gusts over 140 mph and up to 50 inches of snowfall in the mid-Atlantic region of the United States. The storm surge generated was only 20% smaller than Hurricane Sandy (13% smaller after removing the trend in sea level). However, the 1950 storm had a lower overall water level and caused less damage than Sandy because the greatest surge occurred close to low tide. The timing of this event in the tidal cycle was a matter of chance, and thus there is the possibility that ETCs could produce coastal impacts of similar magnitude to those produced by Hurricane Sandy.

1.2. Relationships with large-scale modes of climate variability

Important influences on storm and surge climatology in the northeastern United States include large-scale modes of climate variability (Grise et al. 2013). There has been extensive research on the impacts of El Niño Southern Oscillation (ENSO) on ETCs and associated surge. ENSO warm events are positively correlated with storm surge > 0.3 m during the cool season owing to the meridional displacement of the subtropical jet (Sweet and Zervas 2011), which enhances the East Coast storm track (Eichler and Higgins 2006). Colle et al. (2010) also found an influence of ENSO on observed climatological frequency of minor- and moderate-surge events at The Battery. Other large-scale teleconnection patterns may influence surge frequency, such as the Pacific-North American (PNA) pattern, Arctic Oscillation (AO), and North Atlantic Oscillation (NAO). The positive phase of PNA exhibits below-average geopotential heights over the eastern United States and is associated with an increase in deep-cyclone activity (Gulev et al. 2001). During a negative AO (also referred to as the Northern Hemisphere annular mode), there is a higher frequency of blocking days and frozen-precipitation events in the North Atlantic Ocean (Thompson and Wallace 2001). Negative NAO conditions are also associated with blocking episodes (Shabbar et al. 2001) as well as increased ETC frequency in the western North Atlantic (Teng et al. 2008) and greater storm-tide variability in New York Harbor (Talke et al. 2014).

1.3. Limitations of historical datasets

Understanding the climatology of ETC-driven surge events is important for evaluating

the future risk of inundation events, particularly as sea level rise continues. However, quantifying the risks of high-impact ETCs remains difficult, as examples of such storms are rare in the observational record. High-quality observations for synoptic-scale events that incorporate satellite data are available extending back to the onset of the modern reanalysis era (1979), and the longest tide gauge records span approximately 100 years. Therefore, it is highly unlikely that the most extreme ETC-driven storm surge events that are physically possible are captured in either of these records.

One approach to address the limitations of observational data is to develop a larger sample of ETCs through statistical modeling. Numerous models have been developed for tropical cyclone (TC) hazard assessments (Emanuel et al. 2006; Hall and Yonekura 2013). Lin et al. (2012) analyzed storm surge risk in New York City using a statistical-deterministic model to generate a large sample of TCs. The larger population of TCs included surge-producing storms that do not appear in observations but may be possible, dubbed "grey swans" (Lin and Emanuel 2016). To examine the risks posed by ETCs, Hall and Booth (2017) developed a statistical-stochastic model trained on historical ETC tracks (1979–2015) to estimate rates of severe ETCs in North America, which included grey-swan-type events. However, the model does not simulate wind fields, so impacts associated with severe winds such as storm surge cannot be considered. Large samples of ETCs that also include meteorological information for hazard assessment can be obtained from three-dimensional models of the atmospheric general circulation. A long (i.e. multi-century) simulation of current climate conditions from a coupled atmosphere-ocean general circulation model would provide a better opportunity to sample the tail of

the distribution of high-impact ETC characteristics including severe winds and low central pressures. A longer record also enables an assessment of circulation features during storm surge events that are more extreme than previously observed.

1.4 Scientific objectives

This body of work addresses three principal questions:

1) *What are the similarities in the synoptic evolution of ETCs that generated a large storm surge in the northeastern United States, and how do large-scale atmospheric circulation patterns influence these events?*

We examine the local, regional, and large-scale atmospheric circulation accompanying the 100 largest ETC-driven surge events at three locations along the northeast coast of the United States: Sewells Point (Norfolk), Virginia; The Battery (New York), New York; and Boston, Massachusetts. A statistical analysis of the conditional probability of surge given the large-scale atmospheric circulation is also explored. By comparing circulation patterns of surge-producing ETCs and the conditions under which they occur, we provide a comprehensive evaluation of atmospheric properties associated with the largest observed storm surge events.

2) *What is the potential value of a physically-based sample of high-impact ETCs that is much larger than can be obtained from historical records?*

The utility of using a long integration from a general circulation model to analyze the most extreme impacts associated with ETCs is demonstrated. In exceedance probability estimation of extremes at The Battery, uncertainty is reduced using a longer record rather than records of historical-length. Circulation features associated with a select set of unique high-impact events are also examined to reveal types of ETCs that have not been observed but are physically possible. The examination of a larger sample of high-impact ETCs indicates the potential for more extreme cyclones as well as a greater number of intense storms than have been previously observed, although model biases preclude a quantitative assessment.

3) *How does a regression model developed to identify ETC-driven storm surge events in the northeastern United States perform on a general circulation model?*

Modified regression-based storm surge indices are applied at Sewells Point, The Battery, and Boston to estimate simulated storm surge. Local circulation patterns associated with the largest storm surge index events are compared with features of clustered observed surge events. We also employ a coupled circulation-wave model to evaluate select cases of large surge index events. This work supports the efficiency of using a regression model to identify potential storm surge events in a long record, although a circulation-wave model may provide more accurate surge estimates.

CHAPTER 2

Synoptic Characteristics of Surge-Producing Extratropical Cyclones along the Northeast Coast of the United States

2.1. Introduction

We expand on previous work by analyzing aspects of the large-scale atmospheric circulation associated with surge-producing ETCs. We use observations collected from tide gauges to obtain the highest storm surge levels at our chosen locations, and we use a reanalysis product to analyze accompanying atmospheric circulation for these events. First, local circulation patterns are clustered to observe similarities among development of large surge events at each location. Second, we explore relationships of surge events with modes of climate variability, which influence regional circulation features. Third, a statistical analysis of the conditional probability of surge given the large-scale atmospheric circulation is explored. Our focus will be on storm surge events that occur in the northeastern United States, although the method could be applied elsewhere. The material in this chapter is primarily from the Journal of Applied Meteorology and Climatology article "Synoptic Characteristics of Surge-Producing Extratropical Cyclones along the Northeast Coast of the United States" by Arielle J. Catalano and Anthony J. Broccoli. Hereinafter, this article will be referred to as CB18.

2.2. Data and methodology

The largest surge events produced by ETCs were selected using NOAA tide gauge records (http://tidesandcurrents.noaa.gov) for three locations: Sewells Point, Virginia; The Battery, New York; and Boston, Massachusetts. These locations were chosen for the length and completeness of records (1927–present, 1920–present, and 1921–present, respectively). Mean sea level trends were removed from the observed water level, with detrending centered on the 19-year epoch 1983–2001, a datum to which gauge measurements are referenced. Surge residuals were calculated by then subtracting the astronomical tide, and the 100 largest surges associated with ETCs were retained. Large surge residuals are designated as surge events whether or not a well-defined cyclone is present, although for the vast majority of cases there is a storm in the vicinity. Storms are classified as tropical or extratropical based on their properties at the time of maximum surge (verified using synoptic weather maps and the National Hurricane Center archive). Only separate storm systems are considered – if the same ETC or circulation pattern produces multiple large surges, duplicate values are discarded. Also, hybrid systems that were either in transition or considered tropical up to 18 hours prior to a large storm surge (such as Hurricane Sandy) are removed from this study. Note that raw tide gauge records sometimes contain spurious data due to human or technical errors. We manually remove these portions at each location before detrending and performing additional analysis.

To investigate the historical climatology of surge-producing ETCs, we require a relatively long dataset with high temporal and spatial resolution and homogeneity. Thus, we utilize the latest ECMWF atmospheric reanalysis of the twentieth century (ERA-20C), which has a horizontal resolution of approximately 125 km, 91 vertical levels, and output

spanning 1900–2010 (Poli et al. 2016), sampled at 6-h intervals (0000, 0600, 1200, 1800 UTC) for the purpose of this study. ERA-20C was chosen rather than the twentieth-century reanalysis produced by NOAA/CIRES because it has greater spatial resolution. Comparisons between CIRES and ERA-20C indicate strong similarities in the areas of interest, suggesting that our results are not sensitive to the choice of ERA-20C. Tide gauge data are hourly, so the closest 6-hourly snapshot previous to the time of maximum surge for a given storm is designated as $t = 0$. This choice is based on previous work that has shown that the maximum wind speed occurs prior to the peak of maximum surge (Colle et al. 2010). For consistency with the temporal duration of the ERA-20C dataset, surge events were selected for the period from the beginning of the tide gauge records through 2010. The 100 largest ETC surge events at Sewells Point, The Battery, and Boston range from 0.731 to 1.657 m, 0.896 to 2.400 m, and 0.800 to 1.912 m respectively. The 10 largest surge-producing ETCs at each location are listed in Table 2.1.

We employ *k*-means cluster analysis (MacQueen 1967) to explore natural subdivisions of the 100 largest surge events. *K*-means has been widely used in atmospheric science to analyze features such as storm tracks (Blender et al. 1997, Xia et al. 2013), seasonal wind events (Leckebusch et al. 2008, Burlando 2009, Clifton and Lundquist 2012), and associated atmospheric quantities such as geopotential height (Michelangeli et al. 1995), temperature, and precipitation (Whitfield et al. 2004).

We cluster sea level pressure (SLP) data because of their utility in depicting the location and intensity of ETCs. Because we are interested in the synoptic evolution of each ETC

surge event, we cluster the combined set of SLP fields at $t = 0$, $t = -6$ h, $t = -12$ h, and $t = -18$ h. We find our chosen time period of 18 h preceding a storm surge to be suitable for capturing cyclogenesis and the duration of low-level flow inducing the surge (particularly for slower storms with a larger fetch). The spatial domain used for clustering surrounds the East Coast and includes almost 650 grid points (Fig. 2.1). The domain is designed to include local atmospheric circulation essential to storm surge development and exclude any extraneous features. Cluster analysis demonstrates some sensitivity to variations in the spatial region, but resulting cluster centroids based on alternate domains are very similar to those displayed in this paper.

SLP values at each grid point from all four 6-hourly snapshots are combined into a vector **x** for each surge event, creating an array of data for *k*-means cluster analysis. The algorithm partitions vectors into *K* clusters by minimizing the sum *S* over all clusters of the Euclidean distance of each vector **x** from its respective cluster centroid *m*:

$$S = \sum_{k=1}^{K} \sum_{i=1}^{N} (x_{i,k} - m_k)^2, \qquad (1)$$

where *N* is the length of vector **x** (which includes grid points from four SLP maps resulting in approximately 2600 elements).

Several classification schemes of ideal cluster separation such as silhouette values and complete-linkage hierarchical clustering were considered in our subjective choice of cluster number (Kaufman and Rousseeuw 1990). These visualizations of the optimal cluster number use the Euclidean distance as a metric of dissimilarity, and are therefore

subject to further examination depending on the number of observations and purpose of the analysis. In our study, these choices were made to avoid having clusters with too few storms (subjectively determined to be less than four). The optimal number of clusters for the 100 largest surge events at Sewells Point was chosen to be six, whereas seven clusters were chosen for The Battery and Boston. A visual inspection of individual surge events assigned to sparsely populated clusters (e.g. cluster 4 at Sewells Point) suggests that nearly all events are well represented by the centroid pattern and amplitude. One limitation is that the average pattern may not represent the synoptic evolution of a large surge event with unique characteristics such as unusual propagation or speed. One example is the "Perfect Storm" of October 1991, which was a late-season tropical cyclone in the North Atlantic Ocean that was absorbed by an ETC and propagated westward toward the northeastern coast of the United States. This unusual track coupled with a well-developed and intense cyclone produced a major storm surge at both Boston and The Battery (third and 10th highest respectively). Although a few ETCs have distinct characteristics that differentiate them from other cyclones, particularly in synoptic evolution and propagation, there are similarities among surge-producing ETCs that a cluster analysis reveals.

The relationship between surge-producing ETCs and large-scale atmospheric circulation is explored. We analyze upper-level circulation and anomalies of geopotential height (GPH) at 500 hPa during maximum surge events. Anomalies are calculated by removing the 5-day running mean of the daily climatological average over the entire record. Surge-producing ETC events are also examined in the context of large-scale modes of climate

variability including PNA, NAO, AO, and ENSO. Time-series of indices of these modes of variability are available from the NOAA Climate Prediction Center and the KNMI Climate Explorer.

2.3. Cluster analysis

Results from the cluster analysis for the 6-hourly evolution of surge-producing ETCs are displayed in Fig. 2.2 ordered from highest to lowest associated median surge (see Fig. 2.4). (Recall that SLP fields at $t = 0$, $t = -6$ h, $t = -12$ h, and $t = -18$ h were used to determine the clusters even though only the $t = 0$ field for the cluster centroid is plotted.) Upper-air circulation influences the development and trajectory of surge-producing ETCs, and therefore GPH fields for all clusters are presented in Fig. 2.3. There are a variety of attributes across all clusters. The average storm track may propagate along the east coast, offshore, or from the Midwest, and some centroids exhibit a weaker cyclone that encounters a strong anticyclone as it progresses. At each location, a few clusters may appear similar, but there are subtle differences.

At The Battery, for example, clusters 3, 5, and 7 depict a storm track with secondary cyclogenesis, and the isobars tend to be stretched out along the northwest-southeast axis (Fig. 2.2). There is a stronger anticyclone coupled with a weaker cyclone originating near the Gulf Coast in cluster 5, however, whereas cluster 7 exhibits pressure systems with the opposite intensity and the primary cyclone is near the Great Lakes at $t = -18$. Cluster 3 has a track that is similar to that of cluster 5, although the average cyclone is

stronger at t =0. Comparison of these three clusters at 500 hPa indicates that the GPH anomalies and negative tilt are strongest for the deeper storm (cluster 7) and the GPH field has a longer wavelength than in the other two clusters (Fig. 2.3). Cluster 5 has the shortest wavelength since a second trough is present around 48°W. The positive and negative GPH anomalies have higher amplitudes in cluster 3 than in cluster 5.

Other clusters at The Battery are more diverse. Cluster 6 depicts an average storm with a center jump at t = –6 and no anticyclone present to the north, whereas cluster 2 is a moderate cyclone with an East Coast storm track. Clusters 1 and 4 are both offshore systems, but the cyclone in cluster 4 is stronger and the anticyclone is weaker. The strength of these features is evident in GPH anomalies at 500 hPa (Fig. 2.3).

A similar analysis of cluster features can be conducted at the other locations. At Sewells Point, clusters 1, 2, 3, and 6 feature the average storm advancing from the southwest to Virginia along the East Coast, although with anticyclones of varying intensity and location (Fig. 2.2). For example, cluster 1 features a strong anticyclone over Maine, whereas cluster 2 has a weaker anticyclone over the North Atlantic. GPH anomalies also differ in strength and location in these clusters, and the wavelength of the GPH field is shorter in cluster 3 than in cluster 2 (Fig. 2.3). The shape of the average storm in each centroid has a west-southwest–east-northeast orientation, whereas at Boston, systems are more symmetrical. ETCs at Boston are also generally better developed than at Sewells Point before and at the time of maximum surge.

Table 2.2 lists the average speed of clustered storms, calculated using 6-hourly storm track centers in the 18 h prior to maximum surge. A cyclone-detection algorithm developed at the Geophysical Fluid Dynamics Laboratory identifies cyclone centers using local minimum SLP, and centers are combined into a track through a trajectory analysis (Zhang et al. 2017; Zhao et al. 2009). The criteria for cyclone detection is as follows:

- The requirement of warm core structure is deactivated.
- The minimum lifetime requirement is set to 24 h.
- A SLP minimum with at least one closed 4-hPa contour is required.

The 6-hourly propagation speed is calculated using the difference between a cyclone's current position ($\mathbf{x}_{t=0}$) and previous position ($\mathbf{x}_{t=-6}$) measured along great circles. For the period 1920–2010, the average propagation speed for all cyclone tracks during the cold season (November–April) in a region surrounding the three locations (30º–40ºN, 82º–64ºW) is 13.8 m s^{-1}.

For Sewells Point, all clusters have speeds slower than the average speed of all storm tracks (Table 2.2). Cluster 1 has the slowest average ETC propagation speed, with the centroid exhibiting a strong anticyclone (Fig. 2.2). Storms propagating more quickly near The Battery originate in the Midwest at $t = -18$ (clusters 3, and 7), and slow-moving systems remain offshore and are also inhibited by a strong anticyclone (clusters 1 and 4). In Boston, strong anticyclones are associated with a stationary cyclone offshore (clusters 1, 2, and 3), whereas faster-than-average storms travel northeastward along the coast (clusters 4, 5, and 6).

The largest surge events are divided among the clusters, although some clusters contain more of the higher surges (Fig. 2.4). At Sewells Point, the cluster with the highest median surge (Fig. 2.4a) consists of a strong anticyclone and a slowly progressing cyclone (Table 2.2) that developed within 48 h of the maximum surge ($t = 0$). Cluster 6 has the lowest median surge, and all the surge events in cluster 5 are below 1 m. The two highest median surge values at The Battery (Fig. 2.4b) belong to clusters in which over 75% of the surge events are above 1 m. These centroids exhibit a strong anticyclone and a slow-moving cyclone with an East Coast storm track originating off the southeastern coast at $t = -18$ [a common storm track for large surge events also observed by Colle et al. (2010)]. The top three clusters at Boston also contain a system that is propagating more slowly than average (Fig. 2.4c, Table 2.2).

To focus on the most impactful events, ETCs associated with the five largest surges at each location are analyzed (Fig. 2.5). These surge events are associated with multiple clusters at each location, yet they are well represented by the associated centroid pattern (Fig. 2.2). The strongest surge-producing cyclones occur at Boston, where all five ETCs deepen to an average of 984.4 hPa by $t = 0$. The average central pressure of the top five storms at The Battery is 987.6 hPa, while at Sewells Point the average is 990.2 hPa. All but one of the surge events encounter a strong surface anticyclone to the north with positive GPH anomalies at 500 hPa. Also, these same ETCs propagate more slowly than average in the 18 h prior to maximum surge, with speeds ranging from 3.5 to 13.3 m s^{-1}. This result agrees with our cluster analysis, which indicates that centroids of clusters with

the highest surge events feature a slow-moving system to the south of a strong anticyclone. The similarity of the characteristics of the five largest surge events to those of the cluster centroids suggests that the cluster analysis is successfully identifying patterns associated with large surge events.

2.4. Teleconnection patterns

Teleconnection patterns can affect the regional circulation associated with surge events. The influence of large-scale modes of climate variability on surge events is assessed by examining the frequency distributions of AO, NAO, PNA, and ENSO index values for the top 100 surge events at each location. Daily indices for AO, NAO, and PNA are obtained from the NOAA Climate Prediction Center (at http://www.cpc.ncep.noaa.gov/products/precip/CWlink/). These time series extend back to 1950, so only the events occurring from 1950 to 2010 are included in this analysis (reducing the number of events to ~70 at each location). A monthly Niño-3.4 Index for ENSO spanning 1920 – present is available from the KNMI Climate Explorer. Niño-3.4 is calculated using SST anomalies over a region of the Pacific Ocean, and the index is commonly used to monitor and analyze ENSO conditions (Trenberth and Stepaniak 2001; Chen et al. 2004).

The majority of surge events at The Battery and at Boston occur during the negative phase of the AO, whereas the relationship between surge events and the AO at Sewells Point is unclear (Fig. 2.6a). The influence of the AO on surge events increases from

south to north, with nearly 75% of surge events at Boston occurring during a negative phase of AO. The relationship with NAO is similar although not as pronounced, and there is a positive shift in the frequency distribution at Sewells Point (Fig. 2.6b). The median PNA value is positive at all three locations (Fig. 2.6c), indicating that top 100 surge events are more likely when the PNA is in its positive phase, which is associated with an amplified trough along the East Coast. The negative shift in AO and NAO frequency distributions during surge events extends to antecedent conditions for approximately 10 days, and the positive shift in PNA distributions persists for 5 days (not shown). This persistence is generally consistent with the time scales of AO, NAO, and PNA as determined by Feldstein (2000).

The statistical significance of these shifts in frequency distributions is analyzed using two methods: a two-tailed Student's *t*-test with a hypothesized population mean of index values equal to zero, and a bootstrap analysis in which index values are randomly sampled *N* times with replacement and averaged (where *N* is the total remaining indices at each location for 1950–2010). This process is repeated 1,000 times to generate a distribution of 1,000 sample means and a 95% confidence interval is determined as the 2.5th and 97.5th percentiles of this distribution. If a confidence interval does not include zero, the shift in a frequency distribution is deemed significant at the 5% level.

Significant shifts in the frequency distributions of some teleconnection indices are consistently identified by both bootstrap and *t*-test results. The relationship between surge events and AO is statistically significant at the 5% level at Boston and The Battery

but not at Sewells Point. Statistically significant relationships with NAO and PNA are similarly confined to Boston and The Battery. The negative phases of NAO and AO are generally associated with anomalous positive GPH over southeastern Canada, which are evident in the majority of clusters (Fig. 2.3) and the top five storms (Fig. 2.5) at Boston and The Battery.

Using a statistical–stochastic model based on reanalysis cyclone tracks, Hall and Booth (2017) determined that a negative NAO is associated with slower tracks, which supports our cluster-analysis results that centroids associated with the highest median surges exhibit slow-moving ETCs. Hall and Booth (2017) also observe that positive NAO is associated with enhanced rate of ETCs in the mid-Atlantic region. However, their approach differs because they analyze extreme ETCs (a central SLP anomaly of < -50 hPa), whereas this work focuses on surge-producing ETCs, which have a range of intensities. A more extensive analysis of track properties for surge-producing ETCs would provide a better comparison with Hall and Booth (2017), but it is outside the scope of this study.

ENSO, a large-scale pattern associated with variations in SST in the tropical Pacific Ocean, can influence atmospheric circulation in the North Atlantic (Sweet and Zervas 2011). Both the two-tailed *t*-test and bootstrap method reveal significance at the 5% level for the positive shifts in ENSO distributions at Boston and Sewells Point at $t = 0$ (Fig. 2.6d). This result suggests that strong surge events at these locations are more likely during the positive phase of ENSO. The relationship between El Niño and large storm

surge may be linked to a southward shift in the subtropical jet over the northeastern United States, which increases storm activity along the East Coast (Sweet and Zervas 2011; Eichler and Higgins 2006). Hall and Booth (2017) also observe enhanced zonal propagation during ENSO, but they also observed a reduction in extreme ETC formation in the Northeast.

2.5. Conditional probabilities

In this section, we investigate the probabilities of substantial surge events conditioned upon different local and large-scale atmospheric circulation patterns as defined by the *k*-means cluster analysis and normalized teleconnection indices. To remove the influence of tropical cyclones, only cold season (November–April) events are considered. A small number of late-season tropical cyclones may remain after this seasonal filtering, but rigorous event-specific screening by manual evaluation of synoptic maps is impractical [e.g., 132,860 maps (four maps per day ×365 days per year × 91 years in the longest tide gauge record)].

To understand the influence of local circulation patterns, we calculate the probability of a large surge (≥1 m), a medium surge (≥0.5 m), and a positive surge (≥0 m) occurring for cyclones that most closely resemble a given cluster pattern (Table 2.3). Using all cold-season 6-hourly SLP data corresponding to the period of available tide gauge data, combined SLP maps (at $t = 0$, $t = -6$ h, $t = -12$ h, and $t = -18$ h) are assigned to one of the previously determined clusters (Fig. 2.2) that they most closely resemble based on the

smallest Euclidean distance from each cluster's centroid. Note that if the distance to the centroid is greater than the maximum distance calculated for previously clustered ETCs (Fig. 2.2), the four-panel SLP map is not assigned to any cluster. The number of unassigned events is two to three times the size of the collection assigned to previously determined clusters, and probabilities of large surge events are substantially lower (i.e. one order of magnitude). These new collections of assigned events, which are based on all possible cold-season SLP patterns, regardless of whether there is a cyclone present, are designated as "superclusters." At Sewells Point, the probability of a large or medium surge is greatest for superclusters 1, 2, and 4. These corresponding centroids to which surge values were assigned depict some of the slowest progressing systems for all centroids (Fig. 2.2). At The Battery, the corresponding centroids of the superclusters with the highest probabilities of a positive, medium, or large surge also exhibit a slow-moving cyclone as well as a strong anticyclone (Table 2.3; Fig. 2.2). In a similar way, centroids at Boston with a slower-than-average cyclone and strong anticyclone have the greatest probabilities of large or medium surges (Table 2.3; Fig. 2.2). Overall, the probability of a positive surge event corresponding to a particular supercluster ranges from 73% to 100% across all three locations.

We also explore the relative risk of a large (≥ 1 m) surge during negative and positive phases of PNA, NAO, and AO in the cold season (Table 2.4). Normalized index values are binned into four intervals {strong negative (≤ –1), weak negative (–1,0], weak positive (0,1], and strong positive (>1)}, and associated daily maximum surge values are calculated (1950–2010). Relative risk is defined as the ratio of the probability of surge

events ≥ 1 m in each index interval to the overall probability of surge events of that magnitude. For example, the risk of a surge exceeding 1 m at The Battery is increased by a factor of 1.86 for AO indices ≤ –1. An enhanced risk (>2.00) occurs during the strong negative phase of NAO at all three locations and during the strong negative phase of AO at Sewells Point and Boston. There is also an enhanced risk of a large surge at Sewells Point for PNA indices in the strong positive interval. Conversely, there is a substantial reduction in the relative risk (<0.50) of a large surge for NAO and AO indices in the strong positive interval at all three locations and for PNA indices in the strong negative interval at Sewells Point.

For the relative risk of a large surge during phases of ENSO, daily maximum surge values are assigned to corresponding monthly indices of Niño-3.4. At all three locations, the relative risk is greatest when Niño-3.4 index values are > 1, and risk decreases at Boston and The Battery as indices become more negative (Table 2.4).

2.6. Discussion

A set of distinct, local circulation patterns associated with the 100 largest surge-producing ETCs in the northeastern United States are identified using the *k*-means clustering algorithm. These events are influenced by a variety of synoptic patterns, including intense cyclones, secondary cyclogenesis, and strong pressure gradients associated with relatively weak cyclones coupled with strong anticyclones. Across all locations, average surge levels associated with clustered ETCs are largest for SLP

patterns that include a strong anticyclone to the north of a cyclone propagating more slowly than the average speed of 13.8 m s^{-1}. In addition, superclusters (created with all 6-hourly SLP data for the cold season) that exhibit these features have the highest probability of experiencing a medium (≥0.5 m) or large (≥1 m) surge. In a similar way, the majority of the largest five surge events at each location are deep cyclones to the south of a strong anticyclone. The strength of these features persists at 500 hPa, where there are positive GPH anomalies overlying the anticyclone. Conversely, clusters associated with the smallest average surge levels generally include fast-moving storms coupled with weaker anticyclones. Approximately 93% of the top five surge-producing ETCs moved more slowly than average up to 18 h prior to maximum surge and experienced GPH anomalies at 500 hPa to the north of the storm.

Large surge events occur preferentially during certain phases of large-scale atmospheric circulation patterns. At Boston and The Battery, AO and NAO are more likely to be negative and PNA is more likely to be positive, with these relationships statistically significant at the 5% level. Surge events are more likely to occur under El Niño conditions, with relationships statistically significant at the 5% level at Boston and Sewells Point. Conditional probabilities of surge events also suggest that large surges are more common when teleconnection indices have a specific polarity. At all three locations, the relative risk of a large surge event occurring is greatest for NAO and AO indices in the strong negative interval (≤ –1), and is smallest for positive indices.

In attempting to quantify relationships between atmospheric circulation and storm surge

events with storm surge defined as the difference between storm tide and astronomical tide, there may be an implicit assumption that the magnitude of the storm surge depends only on the large-scale meteorological conditions. There does exist a small, nonlinear interaction between astronomical tides and storm surge (Lin et al. 2012), which affects surge magnitude; storm surge may be larger for events occurring at low tide than for those occurring at high tide. However, this nonlinearity may be minimal at locations along the East Coast (Zhang et al. 2000), especially when its magnitude is compared with the large surge heights involved in this study.

CHAPTER 3

High-Impact Extratropical Cyclones in a Long Coupled Climate Model Simulation

3.1. Introduction

This work is presented as a demonstration of the potential value of a physically-based sample of ETCs that is much larger than can be obtained from the observed record. After a brief description of the model and methodology, results are divided into three sections. First, we establish the value of using a long integration to analyze the most extreme impacts associated with ETCs. Second, we examine the circulation and propagation of notable high-impact ETCs. Third, we evaluate the realism of simulated ETCs through comparisons with a reanalysis product.

3.2. Data and methodology

The long model simulation utilized is from the Forecast-Oriented Low Ocean Resolution (FLOR) version of the Geophysical Fluid Dynamics Laboratory (GFDL) CM2.5 model (Jia et al. 2015). The simulation is 1,505 years in length, and incorporates radiative forcing and land-use conditions at 1990 levels to represent recent conditions. FLOR differs from the original CM2.5 model (Delworth et al. 2012) by virtue of its lower ocean resolution, which reduces computational expense so that long (i.e., centuries to millennia) simulations can be run. The atmospheric component of FLOR has a horizontal resolution of 50 km with 32 vertical levels, whereas the ocean component has a nominal 1°

horizontal resolution, as in the earlier CM2.1 model (Delworth et al. 2006). Since we are most concerned with atmospheric characteristics of ETCs such as circulation patterns, the difference in ocean resolution should not substantially affect our results. Seasonal hindcasts using FLOR indicate that the model is capable of reproducing geographic features important to ETC development such as large-scale mean flow as well as storm track variability (Yang et al. 2015).

To detect and track high-impact ETCs, we use an algorithm developed at GFDL for TCs (Zhang et al. 2017; Zhao et al. 2009) and modified to include ETCs. Criteria are outlined below:

- Using 6-hourly, instantaneous gridded data, potential storm centers are identified from the local minimum SLP, which has been shown to produce similar results in the western Atlantic Ocean compared to trackers using vorticity (Colle et al. 2013).
- To qualify as a cyclone, the area of low SLP must possess at least one closed contour measured at a maximum of 1021 hPa.
- The system must propagate at least 500 km and have a minimum lifetime of 24 h.

Although other ETC trackers generally apply a minimum distance threshold of 1000 km, we set a 500-km limit. The slowest average propagation speed for clustered ETC-driven surge events in the Northeast is 6.6 m s^{-1} (see Table 2.2). For 6-hourly data and a 24 h minimum lifetime requirement, an ETC propagating at 6.6 m s^{-1} travels a distance of approximately 570 km. Since this is an average speed, the minimum distance is lowered

to 500 km to include all potential high-impact cyclones. In addition, previous studies have applied lifetime thresholds ranging from 12 h to 72 h (e.g., Gulev et al. 2001; Raible et al. 2008; Hoskins and Hodges 2002), but Colle et al. (2013) found 24 h to be optimal in the western North Atlantic. We are most concerned with capturing all significant ETCs, some of which have a short duration, so including brief or weak storms will not affect our analysis.

3.3. Utility of a long integration for estimating probabilities of extreme events

In this section, the utility of the larger record of high-impact events in the FLOR simulation for estimating probabilities of extreme events is explored. To estimate the return periods of the strongest events in the record, we employ the block maxima approach of the generalized extreme value (GEV) theorem (Coles 2001). The most extreme value of the variable in question for each year of the simulation is selected, and a three-parameter GEV distribution is fitted to all 1,505 values using maximum likelihood estimation. We calculate the annual exceedance probability curves and 95% confidence intervals for two measures of high-impact ETCs: minimum SLP and maximum wind speed. Only values that occur during the cold season (November–April) are considered. Exceedance curves for these quantities are also computed for consecutive, non-overlapping 31-year and 100-year portions of FLOR to quantify the spread of 10-year, 50-year, 100-year, 200-year, and 500-year return levels as would be estimated from records of comparable length to reanalysis and tide-gauge datasets, respectively.

For each year of the record, the lowest SLP values occurring within 500 km of The Battery measured along great circles are identified. This region is chosen to contain average ETC positions from clustered SLP maps at the time of maximum storm surge at The Battery (see Fig. 2.2). As a measure of intensity, annual minimum SLP values are subtracted from the global mean SLP, 1013.25 hPa; thus largest positive values correspond to the deepest ETCs. The annual exceedance probability for intensity values is displayed in Fig. 3.1a. The GEV curve corresponds well to the actual distribution of intensity values, although the largest 10-15 events generally lie above the best-fit estimate, suggesting that the distribution of actual extreme SLP values has a fatter tail. The median of GEV estimates determined from the 31-year subsamples of the FLOR simulation (hereafter FLOR31) for a 10-year return level is 52.0 hPa, which is close to the value of 52.7 hPa estimated from the full record. However, at return periods beyond the length of the FLOR31 subsamples, uncertainty in return level estimation increases. For example, the range of FLOR31 estimates of 10-year return levels is 10.1 hPa, whereas the range increases to 28.0 hPa and 66.9 hPa for 100-year and 500-year return periods, respectively. At a 100-year return period, GEV analysis estimates a 95% confidence range of 5.1 hPa for an intensity of 62.6 hPa in the full FLOR record.

The narrowing of uncertainties in return levels determined from the longer record is not surprising, as the full record is longer than all the return periods examined (10, 50, 100, 200, and 500 years). But it is noteworthy that the FLOR31 estimates are systematically biased. At each return period examined, the median value of the FLOR31 return level estimates is lower than the return level estimated from the full FLOR sample. This

underestimation is likely due to the fat tail of the actual distribution. The majority of FLOR31 subsamples do not include the most extreme events that lie above the fitted GEV distribution based on the full record. Thus, an underestimation of the return levels in the FLOR31 subsamples relative to those determined from the full sample, which does contain these most extreme events, would be expected. Similar behavior is found for the estimates derived from the 100-year FLOR subsample, so they will not be discussed further.

The distribution of annual maximum wind speeds within 100 km of The Battery (Fig. 3.1b) demonstrates similar behavior to that of SLP intensity values. All the actual wind speed values are located within the 95% confidence limits of the GEV fit determined from the full FLOR sample, although the GEV curve underestimates the most extreme wind speeds in the record. As observed for SLP extremes, the range of FLOR31 return levels for wind speed increases as the return period increases. The difference between the highest and lowest 10-year return level is 3.0 m s^{-1}, whereas the range for a 500-year return level is 15.8 m s^{-1}. The median FLOR31 return levels are again consistently lower than the full record GEV curve.

A significant impact of ETCs near New York City is the storm surge produced. Storm surge potential of simulated systems is evaluated by applying a surge index developed by Roberts et al. (2015) for The Battery. This regression model assumes a linear combination of the local pressure perturbation of the sea level and surface wind stress components. Persistence of strong winds can augment surge height (Bernhardt and

DeGaetano 2012), so the duration of wind stress over the region is included. Since our model output is 6-hourly whereas the index was trained using 3-hourly data, we determined that a zonal integration period of 18 hours and a meridional period of 24 hours for wind stress components yield the best results at The Battery. The index is applied over a comparable region southeast of The Battery (see Fig. 3.4). Hereafter, an estimated surge value is defined as a storm surge index (SSI).

As in Figs. 3.1a and 3.1b, the spread of FLOR31 SSI values is wider at larger return periods, with a range over 2 m for subsample estimates of a 500-year event (Fig. 3.1c). Unlike wind and intensity distributions, the four largest SSI events lie along the GEV curve. The previous 15 events lie above the fit, yet all SSI values are within the 95% confidence intervals. Median FLOR31 SSI return levels are lower than actual levels estimated from the full record, although the underestimation is small compared to that of intensity and wind distributions. This difference could be a result of an underprediction bias for the largest surge events using a regression-based index (Roberts et al. 2015).

The systematic underestimation of return levels determined from the short subsamples may have important implications for estimating extreme events in the real climate system. If the frequency distribution of FLOR ETCs resembles the distribution of actual ETCs in the region of interest (i.e., has a fatter tail than would be expected from GEV theory), then it would be likely that the return levels of ETC-related extremes of SLP, wind speed, and storm surge estimated from the observed climate record would also be underestimated, with a concomitant overestimation of return periods.

3.4. Characteristics of selected extreme events

We adopt the phrase "grey swans" (Lin and Emanuel 2016) to describe high-impact ETCs that have not been observed but are physically possible. In this section, we describe some broad synoptic characteristics of several cold-season grey swans that would have high impacts at New York: the lowest pressure event within 500 km of The Battery, the highest wind event within 100 km of the same location, and the second largest SSI event from the full FLOR record. (We cannot analyze the largest SSI event from the record because upper-level atmospheric circulation variables are unavailable for that portion of the FLOR simulation). Instantaneous values of upper-level circulation variables were not available from any portion of the run. Thus the analysis employs daily averages, which we determine to be sufficient in resolving general patterns and features.

The lowest SLP value within 500 km of The Battery is associated with a March ETC in model year 1307 (Fig. 3.2). The cyclone deepened explosively to 934.9 hPa, intensifying by more than 55 hPa over 24 hours. This rapid development produced an intense pressure gradient immediately south of the ETC center. The highest 10-m wind speeds, which are greater than hurricane-force, are located in this region of the storm. An examination of upper-level circulation for select days prior to the time of lowest central pressure shows a steep 850-hPa temperature gradient in the region of cyclone intensification over the northeastern United States on March 9th, and a 500-hPa GPH cutoff low, which deepened by 240 m in 24 hours (Fig. 3.5). The ETC formed from the

phasing of two troughs. Ridging in Alaska and northwest Canada on March 4th was associated with a downstream shortwave trough in the northern branch of the 500-hPa flow. This trough phased with a second trough in the southern branch propagating from California, and the resulting feature extended over the entire North American continent by March 6th.

The highest wind event within 100 km of The Battery occurred in December of model year 996, and also developed from the phasing of a short-wave trough near California with a trough to the north (Fig. 3.5). On December 2nd, a trough developed at 130°W with a jet streak to the west, which amplified deepening. As the trough progressed eastward over the Rocky Mountains, it flattened a prevailing ridge and merged with the northern trough. By December 7th, the surface cyclone propagated along the northeast coast, encountering an anticyclone over Maine beneath a ridge at 500 hPa. These elements formed a strong pressure gradient, which produced nearly hurricane-force winds at 31.6 m s^{-1} (Fig. 3.3). For over 36 hours, the prevailing 10-m wind direction near The Battery possessed an eastward component. This orientation, strength, and location of winds generated an SSI of 1.56 m.

The second largest SSI event at The Battery reached 2.09 m, occurring in November of model year 780. This system featured greater than storm-force east-northeasterly winds six hours preceding the time of the maximum index value on November 3rd (Fig. 3.4). SSI values remained above 1 m during this period, which is the level at which a coastal flood warning is issued by the National Weather Service (Colle et al. 2010). The SSI

event encountered a strong anticyclone to the north, producing a steep pressure gradient in the region and reducing the rate of propagation to a 12-hour average of 4.1 m s^{-1}, which is slower than the lowest average speed for clustered ETC-driven surge events in the Northeast (CB18; 6.6 m s^{-1}). The strength of these features is evident at 500 hPa, where large GPH anomalies and a cutoff low are present over five days prior to the time of the maximum SSI value. The development of a strong ridge in the northern branch of the flow leads to the formation of a persistent Rex (or "high-over-low") block (Rex 1950) on November 1st (Fig. 3.5), with 500 hPa height anomalies of more than 480 m near Hudson Bay. This block persists for several days, maintaining a strong pressure gradient between high pressure over eastern Canada and a broad cyclone east of the Carolinas. The associated pressure gradient resulted in gale-force onshore winds in the New York Bight for more than 24 hours. CB18 found that synoptic characteristics such as those found in this event were associated with the majority of the largest observed ETC-driven surge events at The Battery.

3.5. Fidelity of the model

The utility of such simulations for quantitatively assessing the probabilities of extreme ETC impacts depends upon model fidelity. In this section, we compare simulated and observed ETC properties in more detail through a comparison with an atmospheric reanalysis product, CFSR (Saha et al. 2010). CFSR provides continuous data for the period 1979 through 2009, and was used to train and test the storm surge index (Roberts et al. 2015). The native atmospheric resolution is 38 km (T382), but for comparable horizontal resolution to FLOR we use output at 0.5°. Reanalyses have been used

previously to evaluate models with respect to simulated cyclones (Bengtsson et al. 2009; Catto et al. 2011). CFSR compares well with other reanalysis products in the spatial distribution of cyclones (Hodges et al. 2003) and propagation of intense ETCs in the Northern Hemisphere (Hodges et al. 2011). Also, CFSR matches well with upper percentiles of buoy and altimetry wind data, suggesting CFSR is more useful than other reanalysis products for analyzing extremes (Stopa and Cheung 2014). Although CFSR is ultimately chosen, we note that a preliminary analysis of climatological wind speeds over the northwestern Atlantic Ocean shows substantial differences among reanalyses. Ascertaining why these differences exist would be valuable as they can affect the utility of reanalysis products for evaluating the fidelity of a model.

Fig. 3.6 displays spatial cyclogenesis rates and feature densities for CFSR and FLOR. As in Hoskins and Hodges (2002), feature density is computed using all 6-hourly cyclone centers passing through a prescribed grid box, even if the centers belong to the same ETC. This gives more weight to slowly moving cyclones, which have been associated with high-impact events in the northeastern United States (e.g., the "Perfect Storm" of October 1991). Spatial densities are normalized by the total record length (1,505 or 31 years).

Comparisons of cyclogenesis and feature densities indicate similarities between CFSR and FLOR. Both CFSR and FLOR exhibit the highest frequency of cyclone development along the East Coast of the United States and extending along the 40ºN parallel (Fig. 3.6a, c). Feature densities are largest in the northwestern Atlantic Ocean including the Bay of Fundy, as well as a localized maximum over Hudson Bay (Fig. 3.6b, d). Since the FLOR

record is considerably longer than CFSR, model output is also subdivided into consecutive, non-overlapping segments of 31 years to compute the spread across these subsamples [FLOR31, as in section (a)]. CFSR feature densities are within one standard deviation (σ) of FLOR values, whereas ETC frequencies differ by approximately 3σ for the region of highest cyclogenesis rates east of Cape Hatteras.

To further diagnose the inconsistency between simulated and observed ETCs, metrics of storm intensity for cold-season ETCs within 500 km of The Battery are evaluated. For each 31-year period of FLOR, minimum central pressures and maximum 10-m wind speeds associated with ETCs are binned in intervals of 4 hPa or 2 m s^{-1} to obtain the spread of subsample frequencies, which are then compared against CFSR frequencies. In over 50% of the bins, the frequency of CFSR wind speeds lies within the 25^{th} to 75^{th} percentile range of FLOR31 values (Fig. 3.7a). However, at several higher wind speed intervals such as 24–26 m s^{-1} and 28–30 m s^{-1}, CFSR values lie outside the spread of the FLOR31 subsamples. Similarly, the frequencies of observed minimum pressures are within the range of FLOR31 values for ETCs with central pressures greater than 990 hPa, but are lower than the range of FLOR31 frequencies for values less than 980 hPa (Fig. 3.7b). This suggests that although the longer record of FLOR provides more examples of ETCs in each wind and pressure interval, as well as values that are more extreme than observed, the model simulates too many intense ETCs.

Because the storm surge index is a combination of central pressure and low-level wind values, biases in the simulation of these quantities may also affect SSI values. Therefore,

the distribution of SSI values for the entire FLOR simulation is compared to the distributions from CFSR and the ECMWF atmospheric reanalysis of the 20th century (ERA-20c; Poli et al. 2016). ERA-20c has a lower spatial resolution than CFSR (125 km), but a longer record spanning 1900–2010. CFSR and ERA-20c data were sampled at 6-hour intervals (00, 06, 12, 18 GMT) for consistency with FLOR output. The additional years of data in the ERA-20c record result in a greater range of SSI values than CFSR, but the distributions are otherwise similar (Fig. 3.8). The spread of ERA-20c SSI values between the 1st and 99th percentiles is 0.96 m with a maximum value of 1.65 m, and the spread for CFSR is 0.86 m with a maximum value is 1.56 m. The SSI distribution for FLOR exhibits longer tails for both positive and negative values, and the maximum index is 2.19 m. However, the spread between the 1st and 99th percentiles is wider than observational datasets, with a range of 1.3 m. The longer FLOR record contains a greater number of large SSI values, but the larger spread of the distribution suggests that FLOR simulates more extreme SSI events, which is consistent with the apparent biases in the variables used to compute the index (10-m wind speed and SLP).

Vecchi et al. (2014) documented a cold bias in FLOR SSTs, which may affect the quantities analyzed in this study. To test the effects, we use an available 500-year 1990 control simulation using a flux-adjusted version of the model (FLOR-FA). FLOR-FA modifies momentum, freshwater, and enthalpy fluxes between the ocean and atmosphere so that the long-term climatology of simulated SSTs resembles observations over the period 1979–2012. When compared with CFSR, normalized cyclone statistics and frequency distributions of intensity metrics in FLOR-FA show a reduced bias relative to

FLOR, but substantial biases remain. As an example of the reduction in bias, annual maximum SLP anomalies in FLOR, FLOR-FA, and CFSR are displayed as a function of return period in Fig. 3.9. Compared to FLOR events, FLOR-FA return values are somewhat closer to those of CFSR, but large differences remain, especially at shorter return periods. A more realistic SST distribution improved the simulation of ETC intensities, but there are still differences in the distribution and magnitude of extreme values when compared to CFSR; this suggests that a systematic bias in the simulation of ETCs exists in FLOR with or without flux adjustment.

3.6. Discussion

Using a multi-century simulation from the GFDL FLOR coupled climate model, we demonstrate the utility of a longer record. The 1505-year simulation includes intense high-impact ETCs that may not be present in a sample of historical-length. Examining a few select FLOR cases, the most extreme ETCs are accompanied by unusually low SLP (934.9 hPa), hurricane-force winds (34.5 m s^{-1}), and a storm surge index value more than 35% larger than the largest computed from reanalysis. ETC events such as these would have potentially severe impacts for coastal regions in their proximity.

Results from an extreme value analysis illustrate that there is a greater uncertainty in estimates of large (> 50-year) return levels for high wind and intensity events near The Battery using 31-year subsamples of FLOR than using the full record. Although this greater uncertainty is not unexpected, the wide range of return levels also suggests the

difficulty in predicting the occurrence rate of high-impact ETCs from shorter records. This has been addressed in previous work examining other extreme climate events in the modeling suite employed here including extreme precipitation events on land (Van der Wiel et al. 2017) and Mississippi floods (Van der Wiel et al. 2018). Perhaps more important, the tendency for return levels to be underestimated when using short (i.e., 31-year) samples has important implications for estimates of ETC impacts using observations. If the distributions of annual maximum wind, intensity, or surge index in the real climate system resemble the model, then statistical analyses using historical records currently available may be underestimating the actual frequency of extreme events.

Comparing the climatological distribution of ETCs in FLOR with a reanalysis product reveals important similarities and differences. The highest frequency of cold-season cyclone development and propagation occurs in the northwestern Atlantic Ocean in both FLOR and CFSR, but the magnitude of the observed cyclogenesis density is nearly three standard deviations higher than the mean FLOR density. Also, minimum SLP and maximum wind speed values associated with simulated ETCs are too frequent in higher intensity ranges compared to CFSR cyclones. Previous work comparing CFSR surface winds with buoys over the North Atlantic identified a slight overestimation in wind magnitude (Stopa and Cheung 2014). This suggests that the differences in ETC intensity between FLOR and CFSR are primarily a result of a model bias in storm strength. Employing a version of FLOR that forces SSTs to be more realistic improves some estimates, but there are still substantial biases present.

CHAPTER 4

Evaluating Storm Surge in a Long Coupled Climate Model Simulation

4.1. Introduction

This section explores the ability of a long simulation from a coupled climate model to realistically simulate atmospheric circulation features associated with the largest ETC-driven storm surge events. We employ a 1505-year record from the Forecast-Oriented Low Ocean Resolution (FLOR) version of the Geophysical Fluid Dynamics Laboratory CM2.5 model (Vecchi et al. 2014; Jia et al. 2015), the utility of which has been demonstrated by previous work (see section 3.3). A multilinear regression model is modified and applied to estimate the largest ETC-driven surge events in FLOR at select locations in the northeastern United States. Then, index performance is assessed through a synoptic analysis of simulated ETCs associated with these events.

4.2. Multilinear regression-based storm surge index

A multilinear regression model (Roberts et al. 2015) is applied to FLOR to identify the largest ETC-driven surge events. This storm surge index is a linear combination of the local minimum sea level pressure P and accumulated surface wind stress components $A\tau_x$ and $A\tau_y$ over a region [Eq. (2)].

$$\text{Estimated Surge}(t) = \beta_0 + \beta_1 A\tau_U(t) + \beta_2 A\tau_V(t) + \beta_3 P(t), \qquad (2)$$

The duration of the zonal (U) and meridional (V) wind stress is included as a spatially-averaged sum over a number of data intervals ($L\Delta t$, in hours) prior to the time of maximum surge [Eq. (2)].

$$A\tau_U(t) = \sum_{i=1}^{L} \overline{\tau_U(t - L_x\Delta t)}, \quad (3)$$

In Roberts et al. (2015), the temporal resolution of data was 3-hourly ($\Delta t = 3$), whereas FLOR output is 6-hourly ($\Delta t = 6$). To estimate storm surge at The Battery in the FLOR record, the integration terms (L_x and L_y) and beta coefficients from the original model were adjusted (see section 3.3). We expand on this work by modifying the index to determine the storm surge potential of ETCs at The Battery and at two additional locations along the northeast coast of the United States: Sewells Point, Virginia; and Boston, Massachusetts. Circulation patterns associated with observed ETC-driven surge events at these locations have been previously evaluated (CB18), which presents an opportunity to compare simulated and observed synoptic-scale features. Since we are interested in storm surge events influenced by ETCs rather than tropical systems, we focus on cold-season events (April–November).

To evaluate the storm surge index model developed at each location, index values are compared to observed surge levels from the NOAA Center for Operational Oceanographic Products and Services tide gauges (http://tidesandcurrents.noaa.gov). To compute surge residuals, hourly water levels measured at the gauges were detrended for sea level changes centered on the 19-year epoch (1983–2001), and the astronomical tide was subtracted. Remaining values represent fluctuations in the ocean surface related to

meteorological influences including wind velocity. Data inconsistencies such as abnormal spikes or tidal shifts are identified and removed (Zhang et al. 2000; CB18). We use SLP and 10-m meridional and zonal wind data from two reanalysis products, CFSR (Saha et al. 2010) and ERA-20c (Poli et al. 2016). CFSR output is 31 years in length (1979–2009) with a horizontal resolution of 0.5 degrees, which is comparable to the atmospheric resolution of FLOR. CFSR was also used by Roberts et al. (2015) to train and test the storm surge index. ERA-20c has a coarser horizontal resolution at approximately 125 km, but a longer record (1900–2010), which enables a better assessment of index performance given the length of available tide gauge records (1927–present, 1920–present, and 1921–present, for Sewells Point, The Battery, and Boston, respectively). For the purpose of this study, data from tide gauge records and reanalysis products were sampled at 6-hour intervals (00, 06, 12, 18 GMT). Overlapping periods for each reanalysis product at each location are used for consistent comparisons with tide gauges. For example, the comparison between tide gauge and CFSR data at The Battery is conducted over the period 1979–2009, whereas storm surge indices using ERA-20c are evaluated against observed surge levels for the period 1920–2010.

The region, integration terms, and coefficients for the storm surge index at each location were chosen based on the highest correlation between observed surge levels and index values. First, index values using coarser ERA-20c data are computed over multiple regions, which are designed to contain relevant wind velocity information (i.e. direction, magnitude, and persistence) from the 100 largest clustered surge-producing ETCs (CB18). Over each region, we test integration periods of the zonal and meridional wind

components from 6 to 48 hours, resulting in 64 combinations. Then, we determine the combination that yields the highest correlation between indices and observed values. The region that produced the strongest correlation is retained for the second phase of screening. In the second phase, the region chosen using ERA-20c is adjusted to correspond to the CFSR native grid resolution. Then, combinations with integration terms from 6 to 48 hours are evaluated. As before, the combination that produces the highest correlation between observed values and indices is selected as the best regression model, and the computed index coefficients, integration terms, and region are retained and applied to FLOR output. The final regions over which the indices are applied are displayed in Fig. 4.1, and coefficient and integration terms are presented in Table 4.1. CFSR terms are also compared with ERA-20c terms from the first phase of screening to examine the dependency of index performance on spatial and temporal resolution. We find that the highest correlation using each dataset involves identical integration terms and similar beta coefficients (not shown). Note that the size of regions chosen influences the surge-producing ETCs identified. The storm surge index SLP term identifies spatial minimum values, whereas the wind stress terms compute a spatial average. Therefore, a larger region would capture a greater number of storm centers, but potentially include winds unimportant to storm surge development at the location of interest. Further analysis of the impact of region selection may be beneficial, such as determining the ability of the storm surge index to identify large surge events driven by ETCs at a considerable distance (e.g., the "Perfect Storm" of October 1991).

Storm surge indices (SSIs) estimated using CFSR data (1979–2009) plotted against

observed surge values illustrate the proficiency of chosen regression models (Fig. 4.2). At Boston, almost all SSI values are within bounds denoting an error of ± 0.5 m, and only a few values are grossly underestimated or overestimated (i.e., beyond 0.5-m bounds). The scatterplot is approximately linear along the 1:1 line, except in the negative tail of the distribution. The nonlinearity in negative values is also a feature of scatterplots at The Battery and Sewells Point, where the index is not as skillful as at Boston. At The Battery, observed storm surge levels above 1 m are estimated to be between 0.4 to 1.6 m by the index, and many negative values are overestimated. Also, the relationship at Sewells Point is not as linear for observed surge values greater than 0.5 m. This suggests that the underlying relationship between low-level circulation and storm surge may not be linear, as assumed by a multilinear regression index. However, the approximation is beneficial for identifying a large sample of sizeable surge events. Future work improving the estimation of simulated storm surge would be useful, but it is beyond the scope of this study.

4.3. Cluster analysis

To characterize natural patterns in the atmospheric circulation associated with the largest SSI events, we perform a *k*-means cluster analysis (MacQueen 1967). *K*-means has been applied previously to cluster storm tracks (Blender et al. 1997), GPH fields (Michelangeli et al. 1995), and SLP (CB18). Since we are interested in the synoptic evolution of storms that produced a large SSI value, we cluster the combined set of SLP fields up to 18 hours prior to the time of the largest SSI value (t = 0 h, t = –6 h, t = –12 h, t = –18 h), over a

comparable domain to CB18 (Fig. 2.1), which surrounds the East Coast. Only separate storm systems associated with the largest SSI values are considered, which are manually identified using associated circulation maps. To facilitate comparisons with clusters of observed surge events, we use the same number of clusters as CB18: seven at The Battery and Boston, and six at Sewells Point.

At each location, the storm surge index is applied to FLOR data, and *k*-means is performed to analyze the circulation patterns of the largest ETC-driven SSI events in a multi-century record. Resulting average cluster patterns, or centroids, at the time of the maximum SSI value ($t = 0$) are displayed in Fig. 4.3, ordered from highest median SSI value to lowest. Cluster patterns at all locations exhibit an average cyclone that propagates along the coast from $t = -18$. The first two centroids at Sewells Point and The Battery contain an average ETC that encounters a strong anticyclone to the north, which tightens the pressure gradient and reduces ETC propagation speed. Average storm speeds are slower than the overall average speed for all observed, cold-season ETCs in a region surrounding the East Coast (13.8 m s^{-1}; Table 4.2). This agrees with the CB18 cluster analysis, in which centroids containing the largest median observed surge levels are associated with slow-moving ETCs near the coast and a strong anticyclone over southeastern Canada (Fig. 2.2). However, the top centroids at Boston do not possess these characteristics. Clusters 4 and 5 exhibit the strongest anticyclones, and clusters 6 and 7 contain the slowest average cyclones (Fig. 4.3). There are also differences in average cyclone symmetry between clustered SSI events and observed storm surge events. As in CB18, most storm systems at Boston are more symmetrical than those at Sewells

Point, which tend to be stretched along the west-southwest–east-northeast axis. However, with the exception of cluster 6, centroids at The Battery do not exhibit a cyclone with a northwest to southeast orientation, which is common among clusters of observed surge events. This difference may be a consequence of biases in the simulation of ETCs, or a bias in identification of surge events using a regression-based index, but additional analysis is required.

At Boston, differences in propagation speed and anticyclone strength between the top clusters of FLOR SSI events and observed storm surge events in CB18 may be related to an inaccurate estimation of surge levels, which are used to arrange the clusters. To illustrate this, the index is applied to ERA20c data (1921–2010), and SLP fields associated with the top 100 SSI events at Boston are clustered (recall that combined snapshots at $t = 0$ h, $t = -6$ h, $t = -12$ h, and $t = -18$ h are used). As in CB18, snapshots at $t = 0$ are the closest maps prior to the time of maximum surge. For each ETC identified using the index, observed storm surge levels are also computed. Centroids are then arranged from highest median SSI value to lowest, as well as highest median observed surge value to lowest to compare the sequence of maps (Fig 4.4). For clusters arranged by median SSI values, centroids containing strong anticyclones or slow-moving systems do not always contain the largest SSI events. However, after arranging clusters by observed surge levels, centroids 1 and 2 exhibit strong anticyclones, and contain an average cyclone that propagates slower than the overall average of 13.8 m s^{-1}. This indicates that the synoptic analysis of the largest SSI events is affected by the ability of the storm surge index to quantify storm surge in the positive tail of the distribution (Fig.

4.2).

Another concern is the inconsistency between observed and simulated surge levels in cluster samples. The lower limits of surge values for the 100 largest SSI events at Sewells Point, The Battery, and Boston are 1.45 m, 1.51 m, and 1.25 m, respectively, whereas in CB18, the lowest values are 0.73 m, 0.90 m, and 0.80 m. To explore the influence of including moderate SSI events in the cluster analysis, *k*-means is performed using SLP snapshots associated with all ETC-driven SSI events above the CB18 limits. This increases the number of individual FLOR events to over 1,700 at each location, but identical cluster numbers are used for comparison. At Boston, resulting centroids (not shown) are qualitatively similar to centroids of the top 100 SSI events (Fig. 4.3), and the sequence of the first four clusters is the same. Also, the strongest anticyclones are not located in clusters containing the largest median SSI values. However, top clusters possess moderately strong anticyclones as well as the slowest propagating cyclones on average. Centroid features for this larger sample of SSI events are more consistent with results from CB18, but this may be related to biases in the storm surge index. Since the index underestimates the majority of observed surges in the positive tail, ETCs associated with SSI values less than 1 m could generate an actual surge that is much larger. Thus, the addition of events with smaller index values to cluster samples may, in fact, include events with actual storm surges much larger than the top 100 SSI values.

4.4. Simulated storm surge levels

To provide more reliable storm surge estimates and explore biases in the storm surge index, we utilize the two-way coupled ADvanced CIRCulation model and Simulating WAves Nearshore model, referred to as ADCIRC+SWAN (Dietrich et al. 2011). Simulations using ADCIRC+SWAN are conducted by Ning Lin and Reza Marsooli at Princeton University. ADCIRC+SWAN is forced with surface wind and pressure fields from SSI events to simulate ETC-driven storm surge along the coast with a five-day spin-up period. Previous work utilized the modeling system of SWAN coupled with ADCIRC to better define hydrodynamics in the presence of meteorological influences (e.g., Dietrich et al. 2012; Hope et al. 2013). SWAN is a spectral wave model that simulates surface gravity waves as they propagate towards the coast (Booij et al. 1999; Ris et al. 1999). ADCIRC is a hydrodynamic model that solves time-dependent, circulation and transport problems along shelves and coasts using unstructured grids (Luettich et al. 1992; Westerink et al. 1994). Storm surge and storm tide simulations have been previously evaluated at a number of coastal regions (e.g., Colle et al. 2008; Lin et al. 2010; Lin et al. 2012). To increase computational efficiency of ADCIRC+SWAN, a ~1 km mesh is applied along the East Coast of the United States, and resulting surge levels are output at 10 minute intervals. For more information on configuration and development, see Marsooli et al. (2018).

Five select SSI values are compared with ADCIRC+SWAN storm surge levels at The Battery. Results show a substantial overestimation by the index at the time of maximum surge (Fig. 4.5). The largest SSI value is 2.19 m and occurred in January of model year 97, but the surge simulated by ADCIRC+SWAN is only 0.87 m. The other selected

surge events also possess index values approximately 1 m larger than modeled surge levels. This is inconsistent with the underprediction bias exhibited by the largest SSIs (determined using winds and SLP from CFSR) compared with observed storm surge levels from tide gauges (Fig. 4.2). The timing of the peak storm surge simulated by ADCIRC+SWAN is within ± 9 h of peak index values, and four of the five modeled surge levels occur following index peaks. The maximum index value for each storm occurs at 120 h, whereas maximum ADCIRC+SWAN surge levels occur at 123 h, 112 h, 123 h, 129 h, and 123 h for events in model years 98, 780, 965, 996, and 1490, respectively. Although there are differences in storm surge height and timing, the shapes of the distributions of estimated and modeled surge over time are similar. For example, following the peak storm surge during the December ETC in model year 996, the index and ADCIRC+SWAN both capture the subsequent fall and rise in surge values, although the amplitude of these features differs. Estimated and modeled surge values are most similar during the February ETC in model year 965, excluding a period of two days around the time of maximum surge.

4.5. Discussion

A storm surge index previously developed by Roberts et al. (2015) to estimate surge events at The Battery is modified to develop indices at two new locations, Sewells Point and Boston. Comparisons of estimated surge levels with observed surge levels at all locations demonstrate the overall proficiency of chosen index models, with correlation coefficients greater than 0.6. We apply the index to the 1505-year record of FLOR to

identify the largest storm surge index events associated with ETCs. At Sewells Point and The Battery, average circulation patterns of the largest events exhibit a strong anticyclone to the north of a slow-moving system, although these features are present in multiple clusters. This agrees with results from a cluster analysis of observed surge events in CB18. The top clusters at Boston do not contain these features, but further examination indicates that the analysis is influenced by errors in storm surge height estimates. Also, almost all centroids at The Battery do not exhibit a northwest to southeast orientation, as in CB18. Differences in cyclone symmetry may be related to biases in the simulation of surge-producing ETCs, which requires further investigation. Cyclone-relative composites of difference fields between FLOR and observations could reveal potential biases in storm structure (Bengtsson et al. 2009; Booth et al. 2013).

The storm surge index underestimates actual surge levels in the positive tail of the distribution at all locations. However, the index identifies a large sample of surge values with low computational demand, whereas methods such as high-resolution hydrodynamic surge modeling can be costly. To explore the utility of a surge model, we perform several case studies using a notable circulation-wave model, ADCIRC+SWAN. The performance of the storm surge index at The Battery is evaluated during five simulated ETCs. The regression model captures the shape of the distribution of surge levels over time when compared with surge model values. However, results show a substantial overestimation by the storm surge index during peak surge levels, which occur prior to almost all maximum surge heights simulated in ADCIRC+SWAN. A potential factor in this overestimation is uncertainty introduced by the circulation-wave surge model, which

must be explored further. An important next step is evaluating ADCIRC+SWAN against observations using meteorological conditions from reanalysis products such as CFSR and ERA-20c. Also, since the computational demand in using a 1505-year record to force ADCIRC+SWAN is considerable, a subset of the largest estimated events could be identified by the storm surge index prior to running ADCIRC+SWAN. Using the index as a screening procedure and analyzing a larger sample of surge-producing ETCs will be the focus of future work.

CHAPTER 5

Summary, Implications, and Future Directions

5.1. Summary

In the northeastern United States, coastal areas have higher exposure to storm surges associated with ETCs than with tropical cyclones (Booth et al. 2016; Orton et al. 2016). ETC-driven storm surge events threaten densely populated, low-lying coastal areas such as New York City. This body of work characterizes the synoptic-scale features and circulation patterns associated with the largest storm surge events at these locations in observations and models.

Chapter 2 expands on previous work concerning regional differences in ETC activity (Zhang et al. 2000; Booth et al. 2015) by analyzing the local, regional, and large-scale atmospheric circulation properties for large ETC-driven storm surge events at Sewells Point, The Battery, and Boston. We develop a framework for analyzing the synoptic climatology of surge-producing ETCs, although our methods are applicable elsewhere. Surface pressure patterns for the clusters containing larger storm surge events exhibit a cyclone encountering a strong anticyclone and propagating slower-than-average. When considering all ETC-driven surge levels, the probability of an event greater than 1 m occurring is highest for clusters with these features. An exploration of upper-air circulation reveals similar patterns in GPH fields during the largest surge events. Also, certain teleconnection patterns, such as negative phases of AO and NAO, have significant

relationships with large storm surge events. Our examination provides an extensive overview of common configurations of circulation associated with observed surge-producing ETCs.

Observational analyses can be limited by sparse or incomplete historical records, so statistical or numerical models are often used. Chapter 3 emphasizes the utility of a long simulation of meteorological data to characterize high-impact ETCs in the tails of the distribution, including storms that produce strong winds, possess low central pressures, or generate large storm surges. In the 1505-year FLOR simulation representing present climate conditions, a greater number of extreme ETCs are identified with higher intensity than observed cold-season storms. Annual exceedance curves of metrics of ETC strength using a record of historical-length rather than the full simulation indicate an underestimation bias in exposure risk. Overall, we outline a modeling approach for more robust statistical analyses of the types of hazardous ETCs that could cause significant impacts. However, comparisons with CFSR reveal ETC intensity biases in FLOR. Thus, this section can be regarded as a proof of concept, the implementation of which will require models with even greater realism.

Although there are intensity biases in FLOR, previous work has evaluated qualitative features of ETC variability against observations (Yang et al. 2015). Therefore, we assess the synoptic evolution of simulated ETC-driven surge events in Chapter 4 using *k*-means cluster analysis. We apply a modified storm surge index to FLOR to identify potential surge events in the northeastern United States. Then, characteristics of circulation

patterns of storm surge index events are compared to patterns of observed surge events using the cluster analysis outlined in section 2.2. Circulation patterns for the largest surge events from the long simulation are qualitatively similar to clustered surge events from observations. However, there are deficiencies in the index, which influence results. There is evidence of underestimation for the largest SSI events compared against actual surge levels (section 4.3), and in exceedance probability curves of annual maximum SSI values at The Battery (section 3.3). However, peak FLOR SSI values are substantially larger than simulated storm surge levels generated by ADCIRC+SWAN during select events. This inconsistency points to potential biases in ADCIRC+SWAN, which requires further investigation. Overall, this work provides the foundation for a more accurate assessment of surge-producing ETCs as physically-based models improve.

5.2. Implications

This research increases understanding of the atmospheric circulation associated with the largest storm surge events in the northeastern United States. An analysis of common circulation characteristics among observed or simulated surge-producing ETCs reveals that the largest storm surge events include a slow-moving cyclone and an anticyclone to the north. This result suggests that strong anticyclones may be particularly important in the development of large storm surge events by inhibiting ETC movement, thus causing a longer duration of onshore winds. Longer duration can lead to an accumulation of water over multiple tidal cycles, which augments surge height (Bernhardt and DeGaetano 2012). Also, the largest ETC-driven surge events in FLOR and observations are scattered among

multiple clusters because of differences in storm development and trajectories. This finding indicates that many types of circulation patterns can influence local development of strong surges. In general, similarities between synoptic characteristics of observed and simulated ETC clusters suggest that results are robust.

One of the novel aspects of this work is the availability of a climate simulation of recent conditions with over 1,500 years of output and 50-km horizontal resolution. Although there are biases in metrics of cold-season ETC development and intensity, we demonstrate that a long model record is useful for a statistical assessment of extreme ETC characteristics and an examination of rare but impactful events that may occur including surge-producing storms. Using the results from FLOR for a robust quantitative assessment of high-impact ETC risks may be precluded by the biases we have found. Nonetheless, results demonstrate that multi-century model runs, should they be of high enough fidelity, could be used to produce more accurate assessments of return levels and return periods for extreme ETCs and their impacts.

5.3. Future directions

Some important aspects of surge-producing ETCs were not addressed and could be a focus of future work. Further exploration of the influences of modes of climate variability on surge-producing ETCs would illuminate the mechanisms involved in these events. The tendency for the top 100 observed storm surge events at Boston and The Battery to occur during the negative phase of AO and NAO and the positive phase of

PNA suggests the importance of the influence of these large-scale circulation patterns on storm tracks and persistence of anticyclones. Recent work by Munroe and Curtis (2017) also establishes a connection between these phases of PNA/NAO and surge duration at Duck, North Carolina. The negative phase of AO/NAO is associated with a southward shift of the Atlantic storm track, which would increase the likelihood of cyclones passing to the south and east of Boston and The Battery. The negative phase of AO/NAO is also associated with more frequent blocking over Canada and the Atlantic Ocean (Shabbar et al. 2001), which may contribute to storm surge events by slowing ETCs and tightening the pressure gradient to their north. The positive phase of PNA can be regarded as an intensification of the climatological trough over eastern North America in the middle and upper troposphere, which would enhance activity in the western portion of the Atlantic storm track. Analyzing the relationship between modes of climate variability and storm surge events in a long model record such as FLOR would be beneficial. A larger sample of surge-producing ETCs decreases uncertainty in statistical analyses such as those applied in sections 2.4 and 2.5.

This dissertation analyzes surge-producing ETCs under present climate conditions. However, an important concern going forward is the impact of anthropogenic climate change on inundation risks to coastal communities. The rate of increase in mean sea level over the past century contributed to an increase in 5- and 10-year return period estimates of storm surge in the New York Harbor region (Talke et al. 2014). Sea level rise is likely to be the dominant contributor to future changes in inundation risk (Roberts et al. 2017, Sweet et al. 2013, Lin et al. 2012), but exploring potential changes in surge-

producing ETC climatology under a warming climate is also important, as changes in storm tracks or intensity could have disproportionate effects on distribution tails. By applying the regression surge index to several CMIP5 models and the CESM large ensemble, Roberts et al. (2017) observe a poleward shift and intensification of ETCs with the potential to produce a large storm surge. Seasonal changes in atmospheric circulation features such as the mid-latitude jet stream, which has been shown to affect storm track variability (Eichler and Higgins 2006; Athanasiadis et al. 2010), have the potential to alter storm surge risks at specific locations. Also, large storm surge-producing ETCs in the Northeast occur preferentially during certain modes of climate variability (i.e. negative NAO, AO) and synoptic-scale circulation patterns (CB18). Whether these circulation features respond to a changing climate will affect ETC propagation and associated impacts on different timescales.

Quantifying storm surge risk requires a comprehensive understanding of the natural variations in surge-producing ETCs, as well as an understanding of the influence of climate change on storm climatology. However, the models used in this work do not adequately simulate all aspects of the climate system. Intensity biases in FLOR affect return level estimates of high-impact ETCs, and estimation biases by the storm surge index affect analyses of atmospheric circulation patterns associated with the largest surge events. As advancements are made in these representations of the climate system and longer records are produced, our ability to identify physical mechanisms influencing surge-producing ETCs and quantify the risks posed by infrequent and impactful events will be realized.

	Extratropical	Tropical
Sewells Point	71	29
The Battery	88	12
Boston	91	9

Table 1.1. Percentage of the 100 largest surge events at Sewells Point, The Battery, and Boston categorized by storm type (i.e., extratropical or tropical).

Sewells Point		The Battery		Boston	
Date (GMT)	**Surge (m)**	**Date (GMT)**	**Surge (m)**	**Date (GMT)**	**Surge (m)**
11/13/2009 03:00	1.657	11/25/1950 20:00	2.400	02/26/2010 04:00	1.912
03/07/1962 19:00	1.558	12/11/1992 17:00	1.809	11/30/1945 08:00	1.526
02/05/1998 02:00	1.503	03/29/1984 14:00	1.587	10/31/1991 02:00	1.488
01/28/1998 22:00	1.388	11/10/1932 05:00	1.547	03/29/1984 19:00	1.383
10/25/1982 12:00	1.357	11/17/1935 21:00	1.478	04/14/1961 00:00	1.381
04/26/1978 23:00	1.286	03/13/1993 22:00	1.476	02/07/1978 08:00	1.380
01/24/1940 08:00	1.210	11/07/1953 10:00	1.459	11/18/1935 02:00	1.350
01/29/1937 10:00	1.208	10/27/1943 04:00	1.429	02/15/1940 03:00	1.270
01/25/2000 11:00	1.200	01/25/1979 02:00	1.418	11/12/1968 19:00	1.238
04/12/1956 07:00	1.192	10/31/1991 09:00	1.414	03/03/1947 06:00	1.233

Table 2.1. The 10 largest storm surges associated with an ETC (detrended for sea level changes), measured at the NOAA tide gauges in Sewells Point, The Battery, and Boston.

	Sewells Point	**The Battery**	**Boston**
Cluster 1	9.2	10.4	7.9
Cluster 2	6.6	10.3	8.8
Cluster 3	11.3	15.9	7.1
Cluster 4	9.7	8.6	14.0
Cluster 5	11.1	14.2	14.2
Cluster 6	9.5	13.8	14.1
Cluster 7	N/A	15.0	10.2

Table 2.2. Average speed (m s^{-1}) of cyclones in each cluster at Sewells Point, The Battery, and Boston. As discussed in the text, the average speed of all cyclones in the region surrounding these locations is 13.8 m s^{-1}.

	Cluster	# Storms	Surge ≥ 0 m	Surge ≥ 0.5 m	Surge ≥ 1 m
Sewells Point	**1**	2,011	83.1	6.7	0.5
	2	1,099	97.5	11.7	1.0
	3	4,739	86.4	4.7	0.4
	4	186	100.0	36.0	5.4
	5	1,167	92.3	4.5	0.0
	6	5,746	73.8	3.4	0.1
The Battery	**1**	717	96.7	16.2	1.7
	2	675	99.4	31.6	4.3
	3	3,451	93.0	8.5	0.4
	4	912	97.4	21.3	2.0
	5	1,631	94.0	10.8	0.7
	6	3,202	87.3	4.6	0.3
	7	5,323	89.7	5.9	0.2
Boston	**1**	404	96.0	17.3	1.7
	2	311	99.4	44.7	3.9
	3	687	99.0	14.1	0.4
	4	1,849	99.6	13.7	0.5
	5	5,114	90.7	5.2	0.2
	6	10,547	91.1	2.6	0.1
	7	3,089	94.0	5.1	0.2

Table 2.3. Probability (%) of surge ≥ 0, 0.5, and 1 m for all events assigned to previously determined clusters at Sewells Point, The Battery, and Boston.

		Index ≤ -1	-1 < Index ≤ 0	0 < Index ≤ 1	Index > 1
Sewells Point	**PNA**	0.27	0.65	0.81	3.00
	NAO	2.17	1.37	0.44	0.48
	AO	2.04	1.08	0.66	0.22
	ENSO	0.40	1.05	0.33	2.68
The Battery	**PNA**	0.57	1.05	0.99	1.38
	NAO	2.51	0.96	0.77	0.26
	AO	1.86	0.80	0.99	0.35
	ENSO	0.33	0.78	1.28	1.63
Boston	**PNA**	0.70	1.45	0.70	1.18
	NAO	2.80	1.18	0.47	0.21
	AO	2.86	0.70	0.45	0.19
	ENSO	0.66	0.77	1.21	1.40

Table 2.4. Relative risk of surge events ≥ 1 m for PNA, NAO, AO, and ENSO index values within four intervals at Sewells Point, The Battery, and Boston. Relative risk is defined as the ratio of the probability of surge events ≥ 1 m in each index interval to the overall probability of surge events of that magnitude.

Location	β_0	β_1	β_2	β_3	L_x	L_y	R^2
Boston	0.0087	–0.3219	–0.0245	–0.0083	1	6	0.625
The Battery	0.0407	–0.2769	–0.0254	–0.0072	3	4	0.642
Sewells Point	0.0140	–0.1919	–0.2763	–0.0076	6	2	0.604

Table 4.1. Values of beta coefficients and integration terms in the storm surge index equation, and the correlation coefficient between CFSR index values and observed surge values at each location.

	Sewells Point	**The Battery**	**Boston**
Cluster 1	5.6	13.2	8.9
Cluster 2	3.4	5.4	9.1
Cluster 3	2.8	7.1	10.0
Cluster 4	7.0	8.0	11.6
Cluster 5	6.8	4.0	10.0
Cluster 6	8.6	8.8	6.0
Cluster 7	N/A	8.2	8.0

Table 4.2. Propagation speed (m s^{-1}) of average cyclones in each centroid for clustered FLOR SSI events at Sewells Point, The Battery, and Boston.

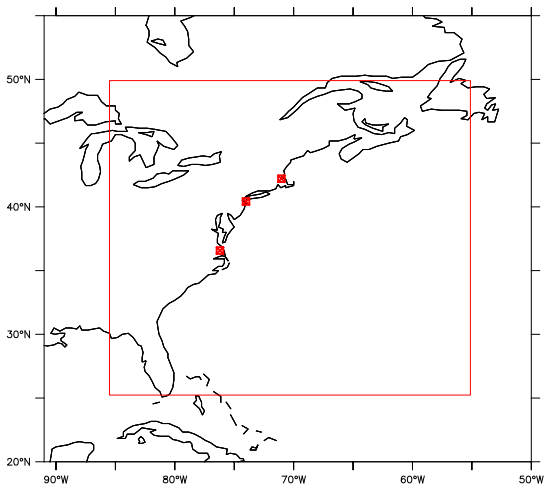

Fig. 2.1. The spatial domain in which *k*-means clustering is performed using ERA-20c sea level pressure data. Red points indicate the locations of the tide gauges at Boston, The Battery, and Sewells Point.

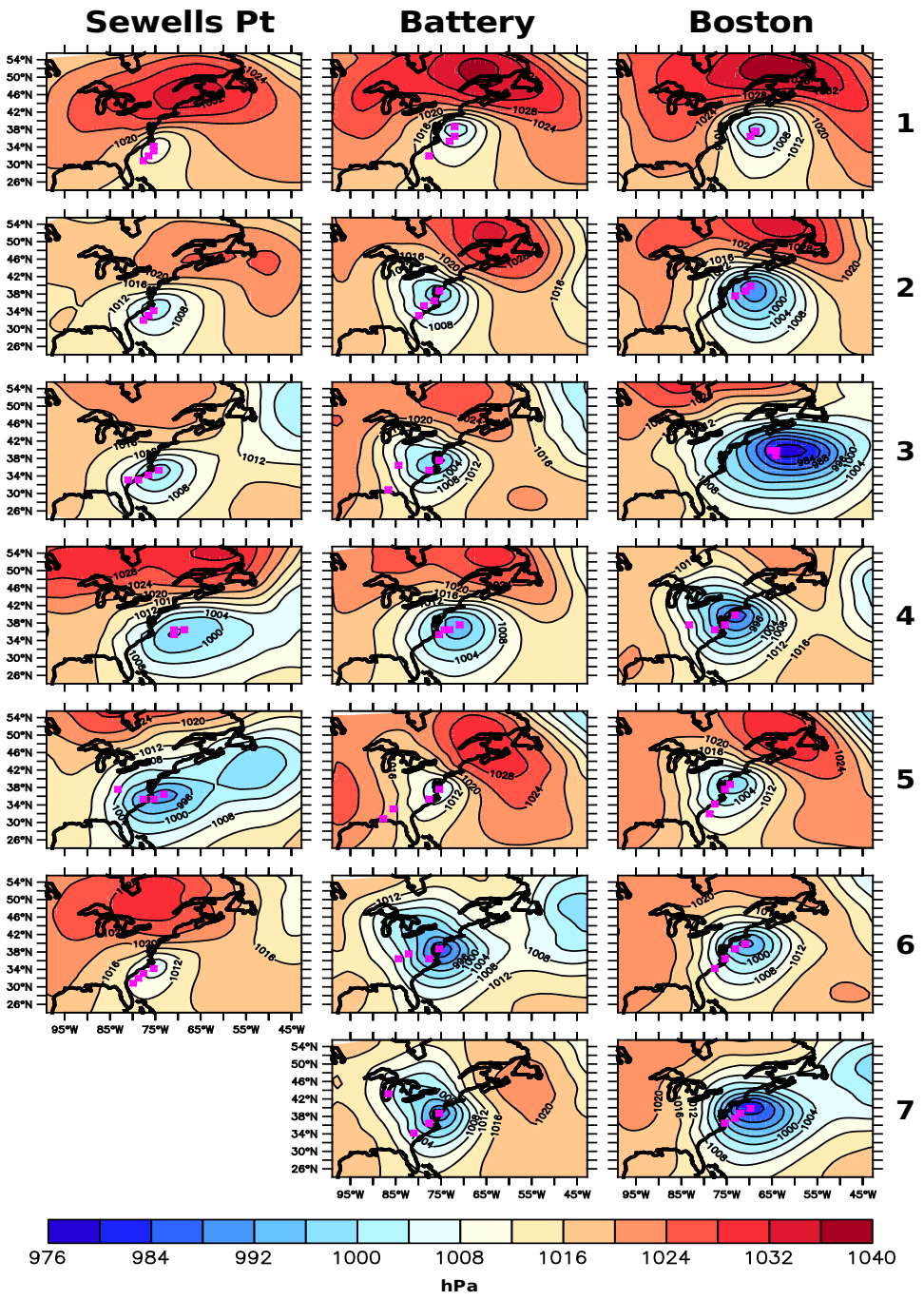

Fig. 2.2. Cluster centroids (numbered from top to bottom on the right-hand side) for the 100 largest surge-producing ETCs at Sewells Point, The Battery, and Boston organized by decreasing associated surge values. Each map depicts the cluster centroid at the time before maximum surge ($t = 0$). Average cyclone centers at 0-, 6-, 12-, and 18-h lags ($t = 0$, $t = -6$, $t = -12$, $t = -18$) are marked in magenta.

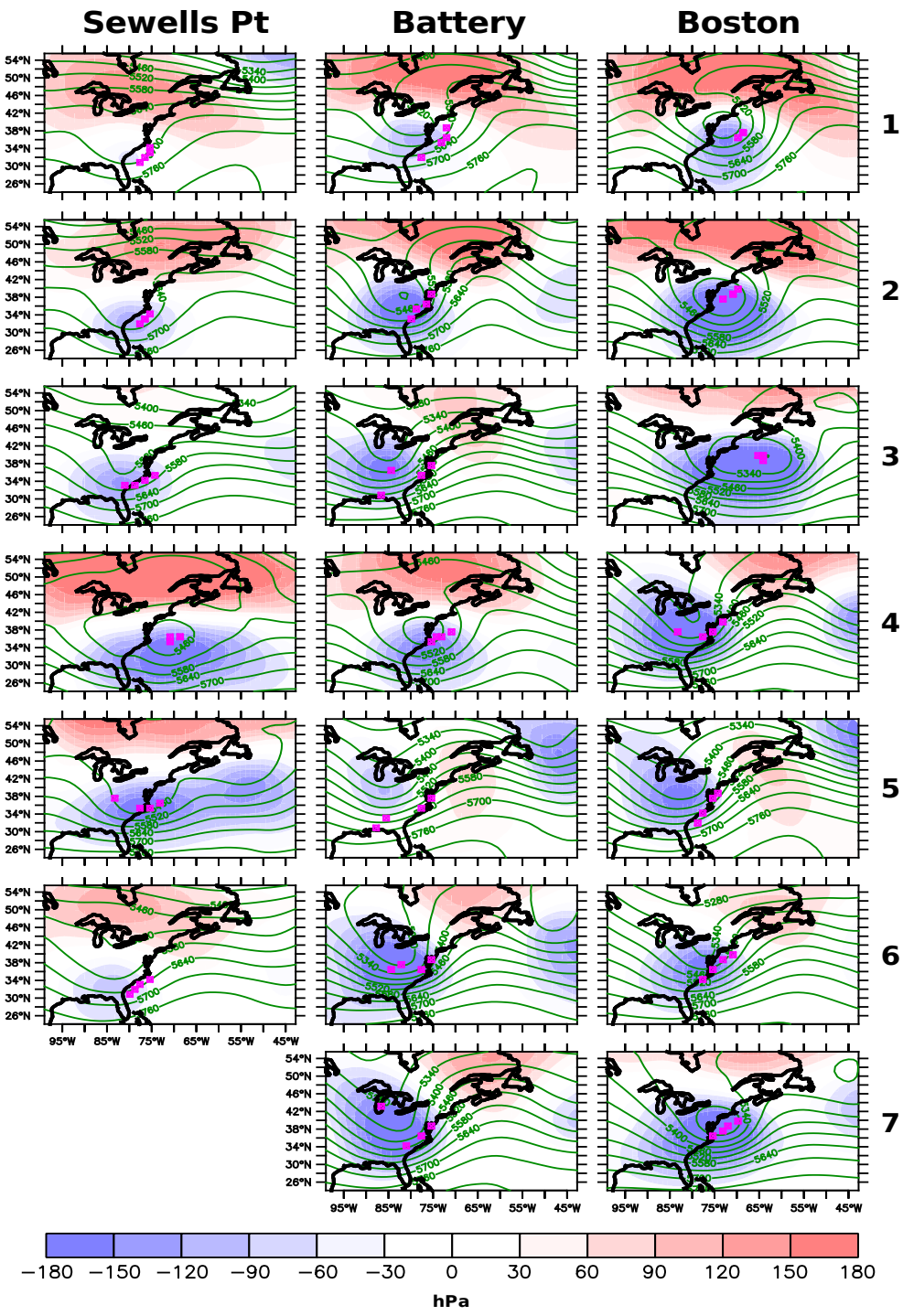

Fig. 2.3. Composite maps of atmospheric circulation at 500 hPa at $t = 0$ for the clusters in Fig. 2.2. Average cyclone centers at 0-, 6-, 12-, and 18-h lags ($t = 0$, $t = -6$, $t = -12$, and $t = -18$) are marked in magenta. Solid green contours represent GPH (m), and shaded regions are GPH anomalies (m).

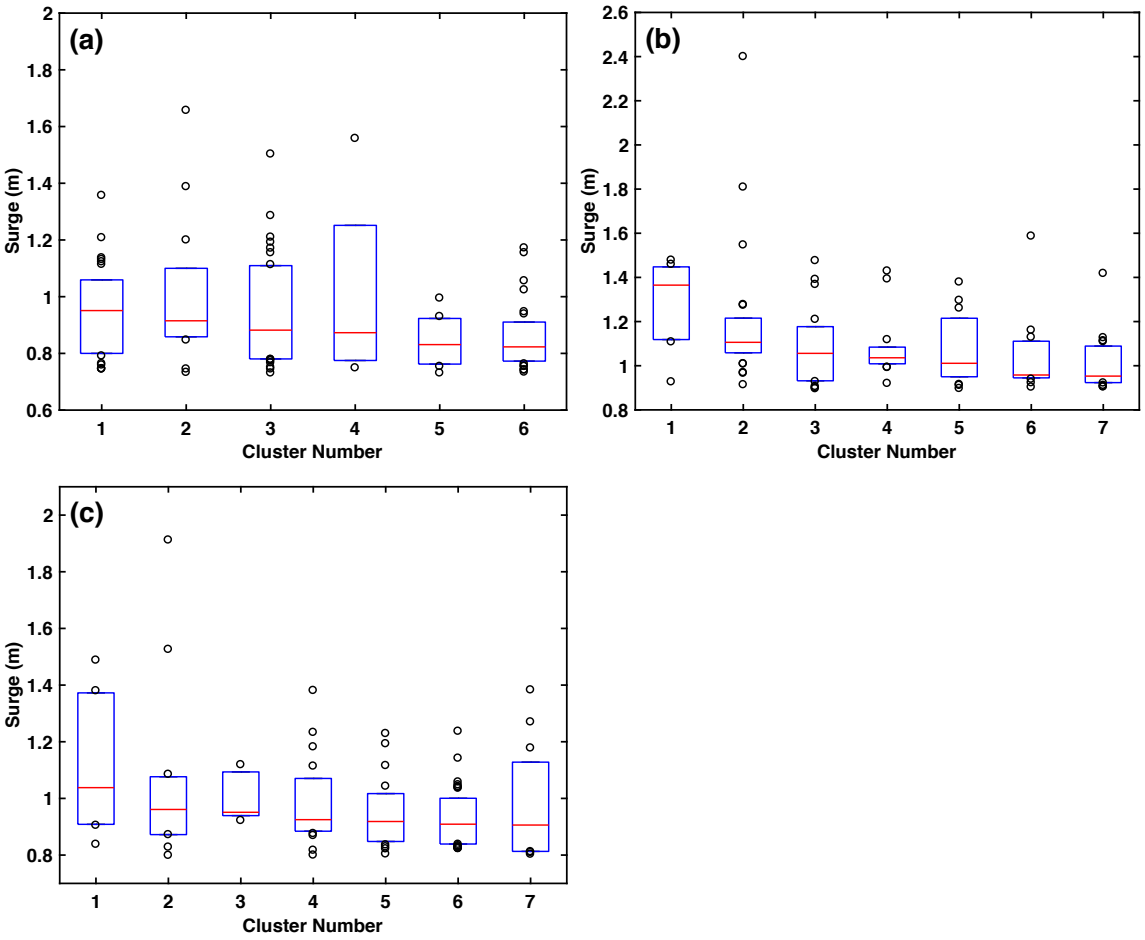

Fig. 2.4. Box-and-whisker plots of surge values (m) associated with the 100 largest ETC events at (a) Sewells Point, (b) The Battery, and (c) Boston organized by cluster. The top and bottom of the boxes represent the 75th and 25th percentiles, respectively, and red lines within each box indicate the median value. Open circles are surge values that lie outside the 25th and 75th percentiles.

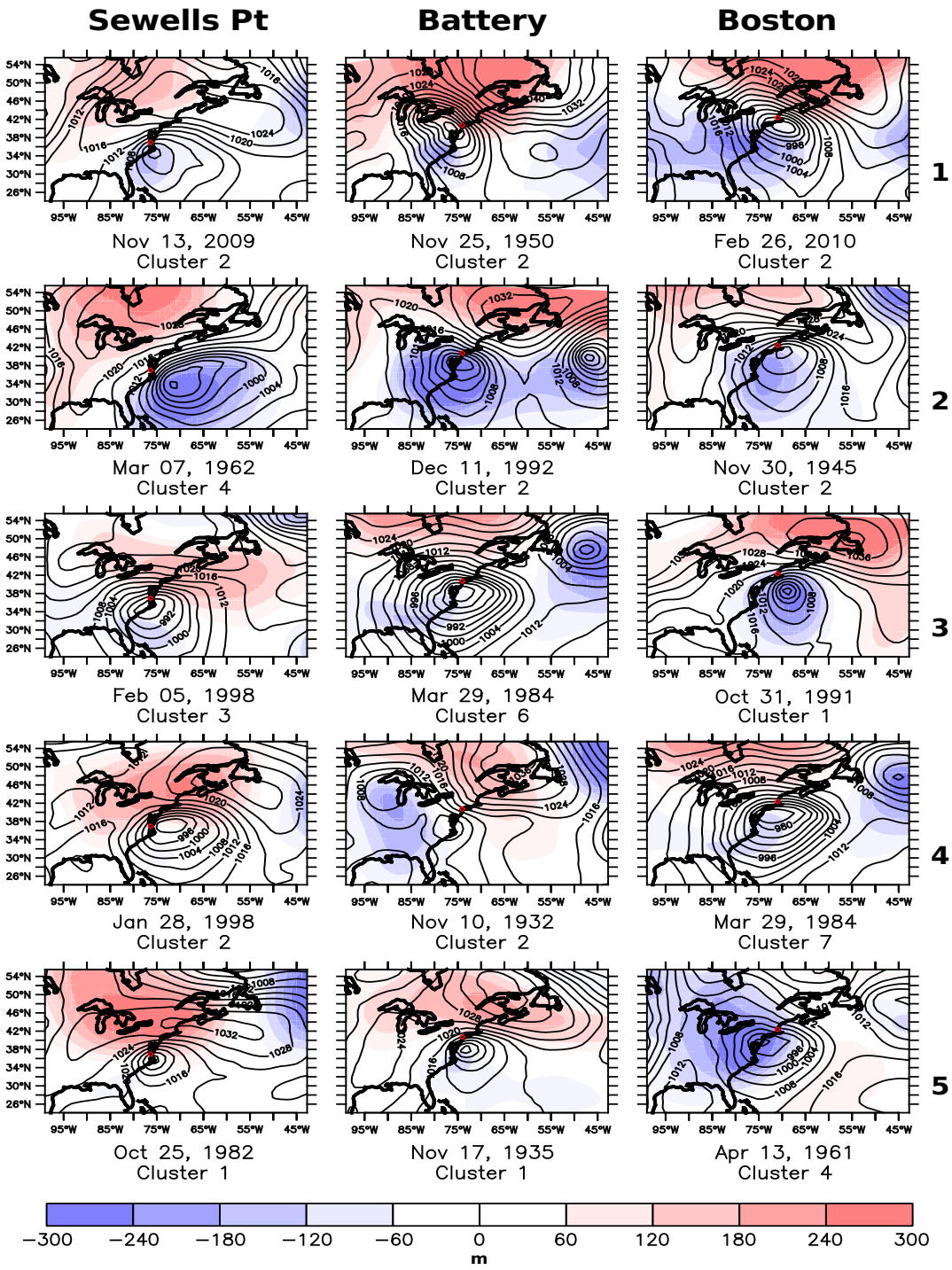

Fig. 2.5. Atmospheric circulation at time before maximum surge (t = 0) for the five largest surge events (decreasing from top to bottom) at Sewells Point, The Battery, and Boston. Solid black contours represent SLP (hPa), and shaded regions are GPH anomalies (m).

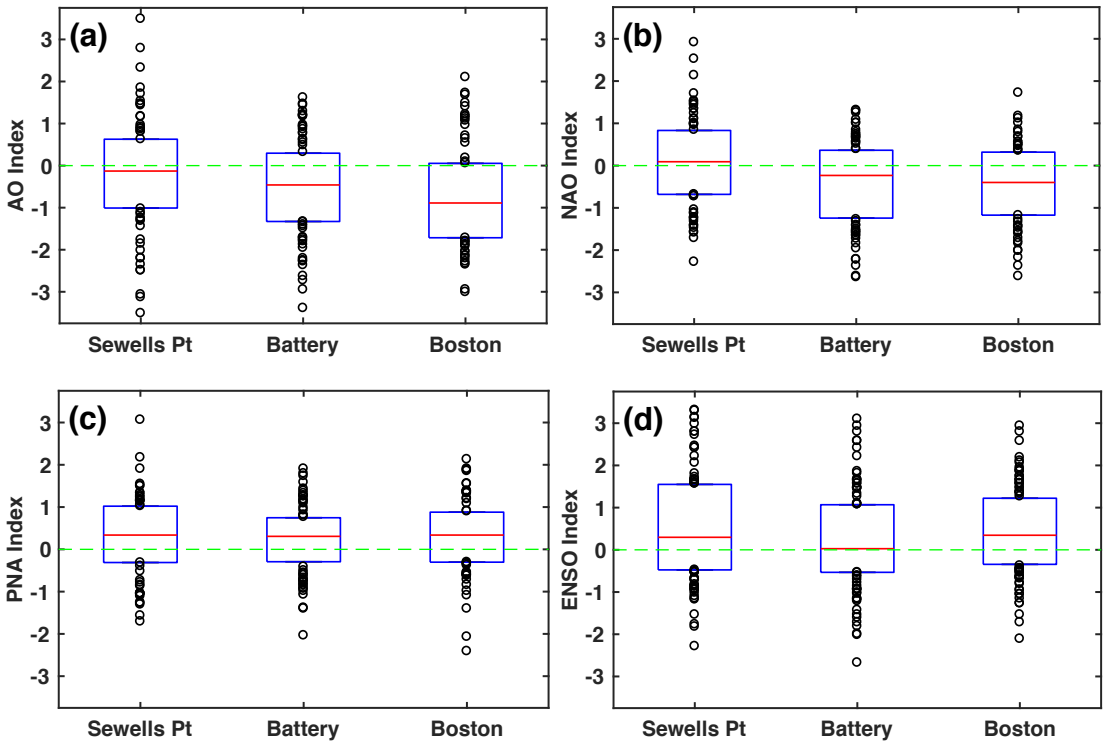

Fig. 2.6. Box-and-whisker plots of (a) AO, (b) NAO, (c) PNA, and (d) ENSO index values for the 100 largest surge events at Boston, The Battery, and Sewells Point.

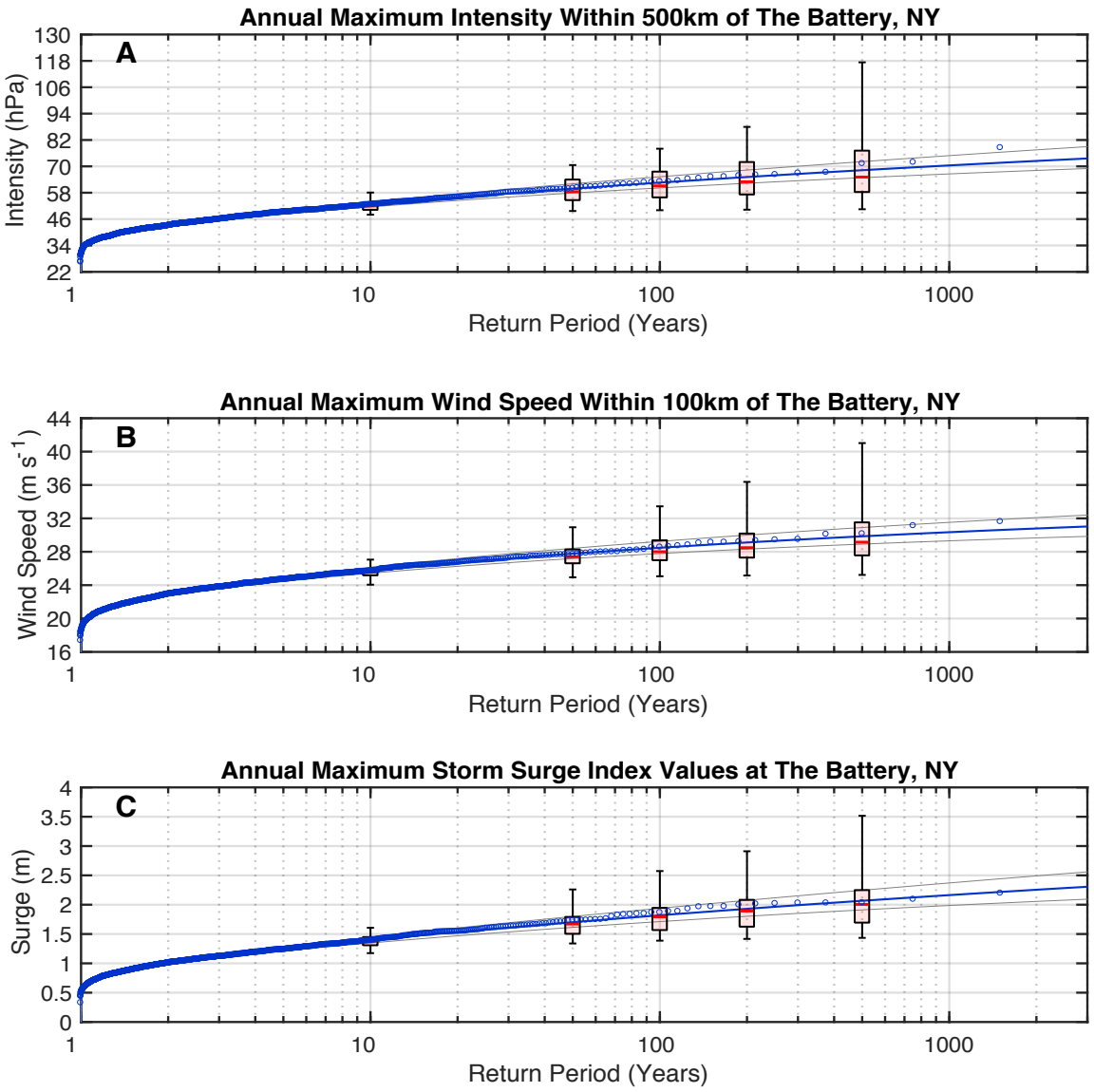

Fig. 3.1. FLOR annual exceedance probability curves of (a) maximum intensity values within 500 km of The Battery (in hPa), (b) maximum wind speed values within 100 km of The Battery (in m s^{-1}) and (c) storm surge index values (in m) at The Battery as a function of return period. Grey lines are 95% confidence bounds on the distribution curve. Box-and-whisker plots indicate the range of estimated values for FLOR 31-year subsamples at designated return periods (10, 50, 100, 200, and 500 years). The top and bottom of the boxes represent the 75th and 25th percentiles, respectively, and red lines within each box indicate the median value.

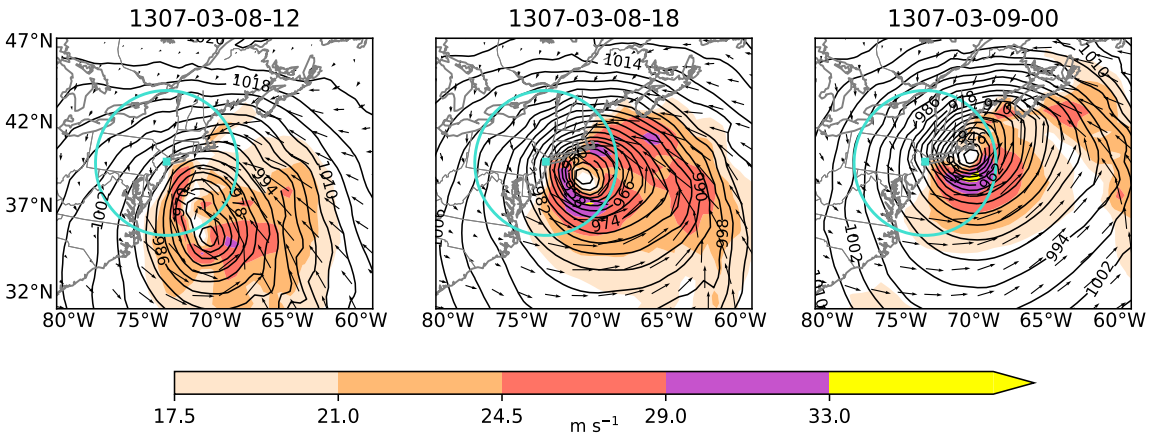

Fig. 3.2. Contoured SLP maps of the deepest simulated ETC during the cold season within 500 km of The Battery (in turquoise). Vector overlay and shaded regions are 10-m wind speeds categorized according to the Beaufort scale wherein 17.5 m s^{-1} is gale, 21.0 m s^{-1} is strong gale, 24.5 m s^{-1} is storm, 29.0 m s^{-1} is violent storm, and > 33.0 m s^{-1} is hurricane-force wind.

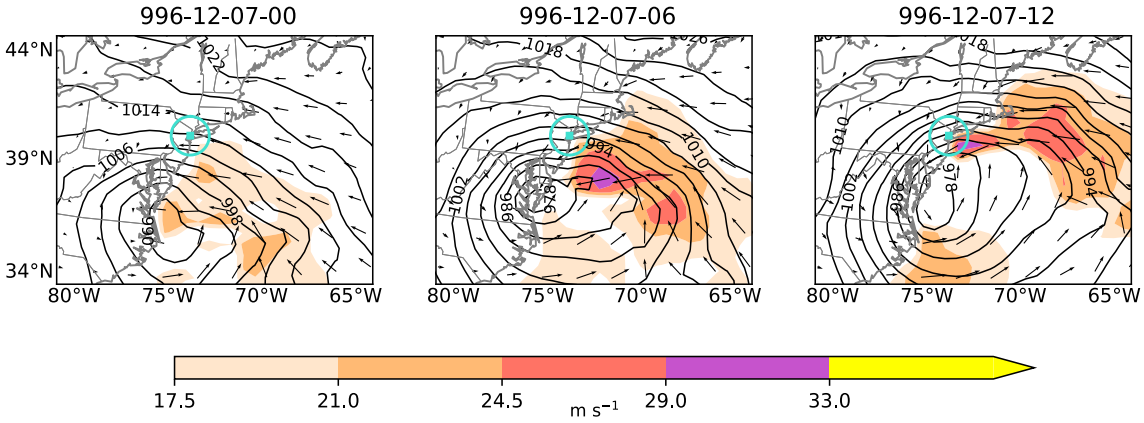

Fig. 3.3. As in Fig. 3.2 but for a simulated ETC associated with the highest wind speed during the cold season within 100 km of The Battery (in turquoise).

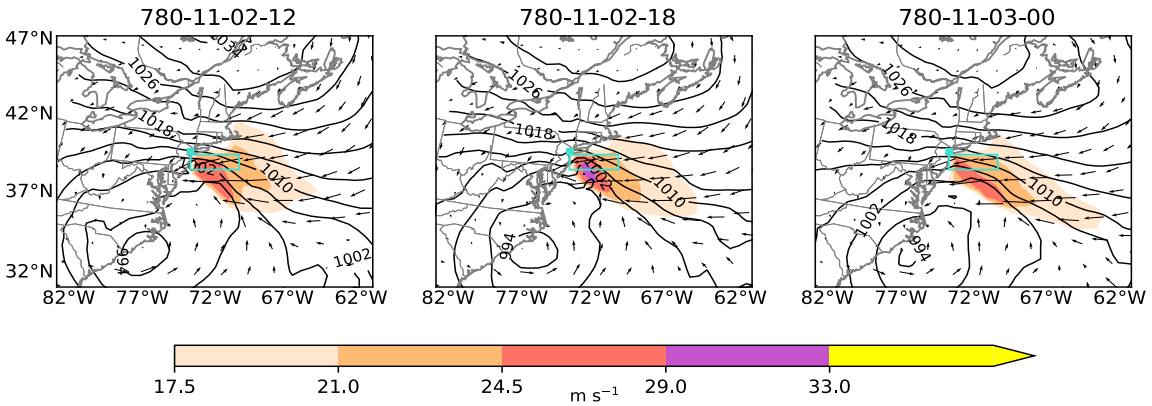

Fig. 3.4. As in Fig. 3.3 but for a simulated ETC associated with the second largest storm surge index (SSI) during the cold season calculated over a region southeast of The Battery (in turquoise). The SSI values from left to right are 1.57 m, 2.02 m, and 2.09 m.

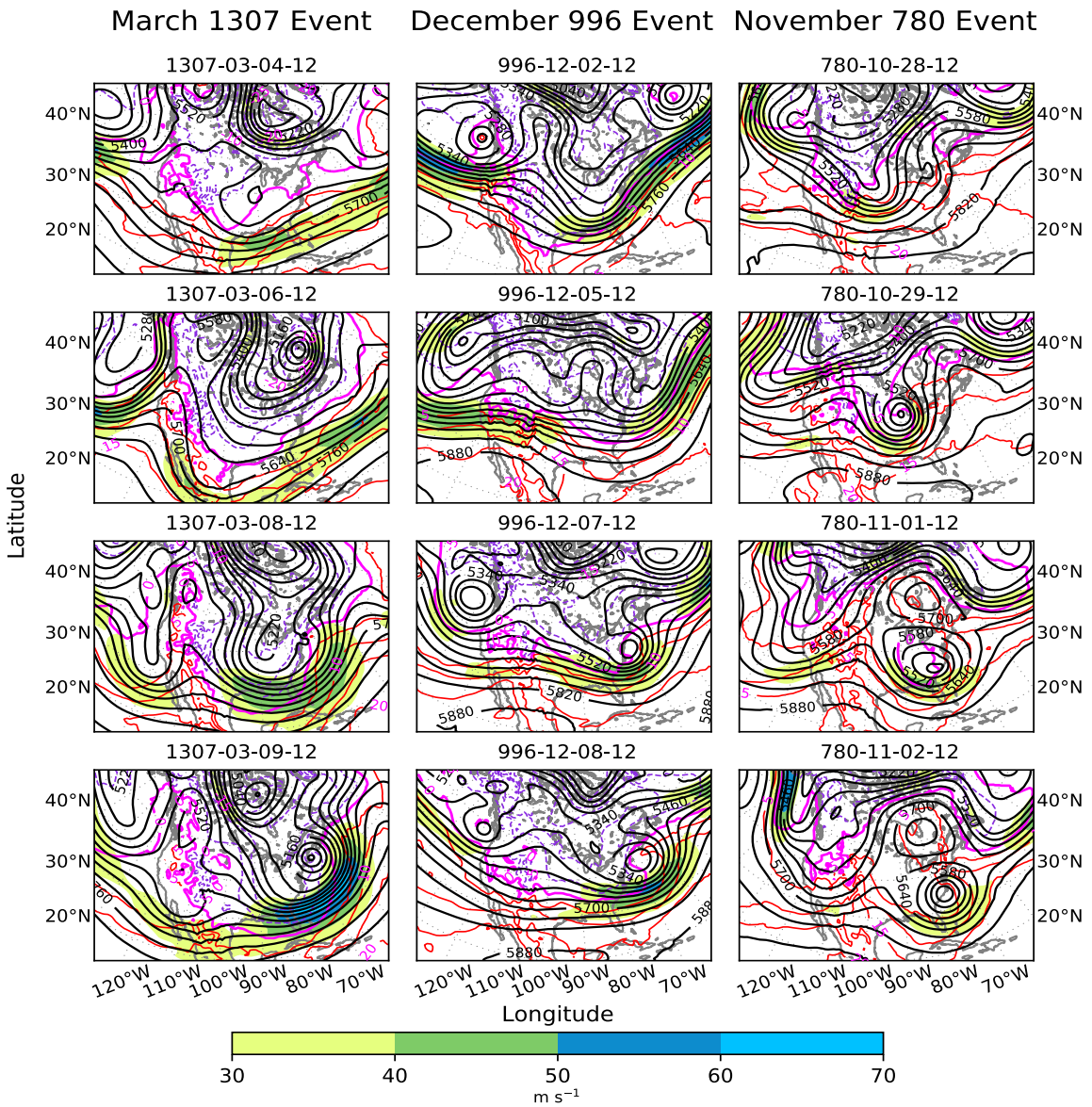

Fig. 3.5. Daily average atmospheric circulation at 500 hPa and temperature at 850 hPa for select days associated with the lowest pressure event (first column), the highest wind event (second column), and the second largest storm surge index event (third column) near The Battery (see Figs. 3.2–3.4). Solid black contours represent GPH (m), shaded regions are wind speeds at 500 hPa (m s^{-1}), and colored contours represent 850-hPa temperature (°C) where solid red are positive values, dashed purple are negative values, and the magenta line is zero. Note, maps increase in time from top to bottom, but intervals between maps differ.

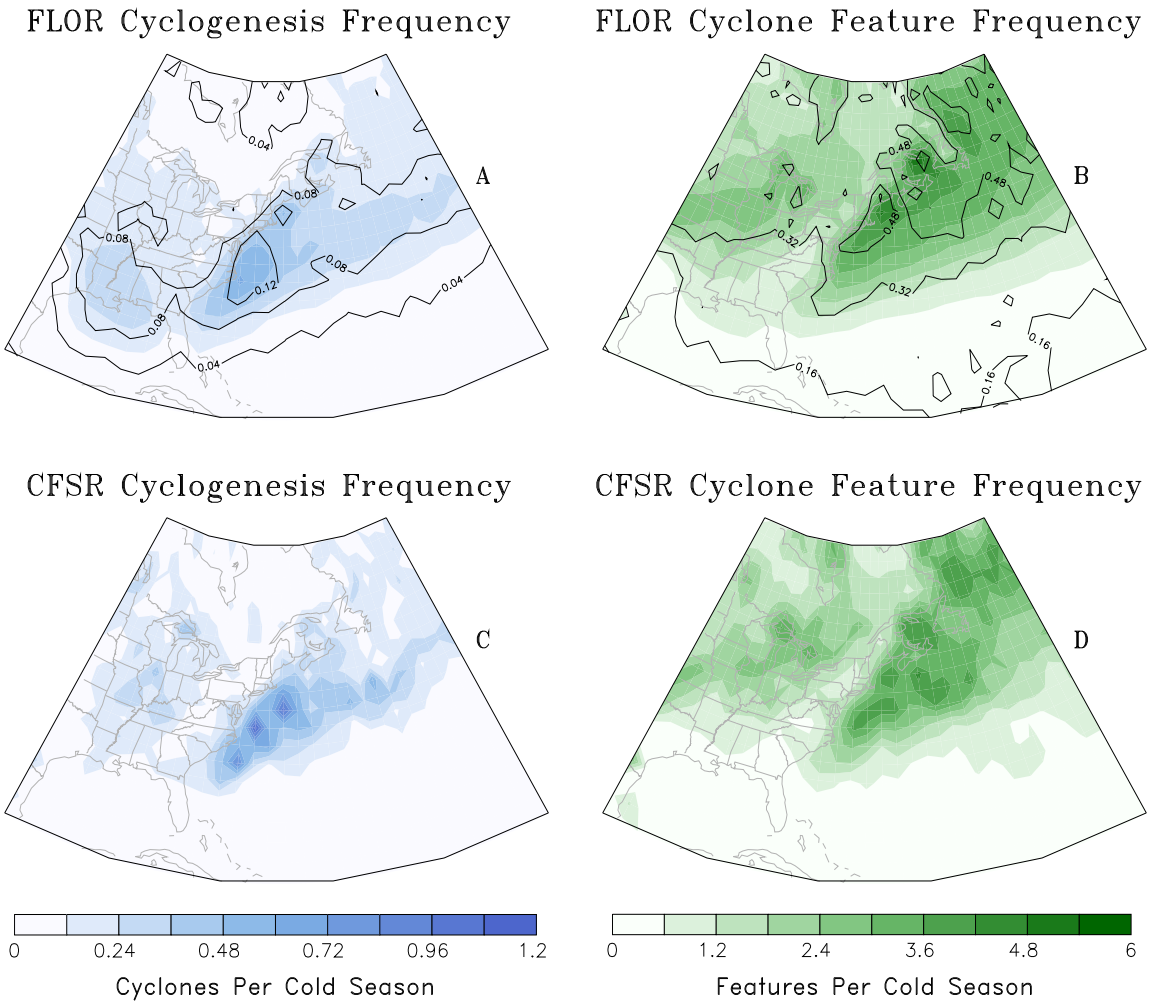

Fig. 3.6. FLOR (a, b) and CFSR (c, d) cyclogenesis and feature densities per cold season normalized by record length (1,505 and 31 years, respectively). Black contours represent one standard deviation spread over 31-year subsets [contoured at intervals of 0.04 (a) and 0.16 (b)]. Feature density measures the number of cyclone centers passing through the region.

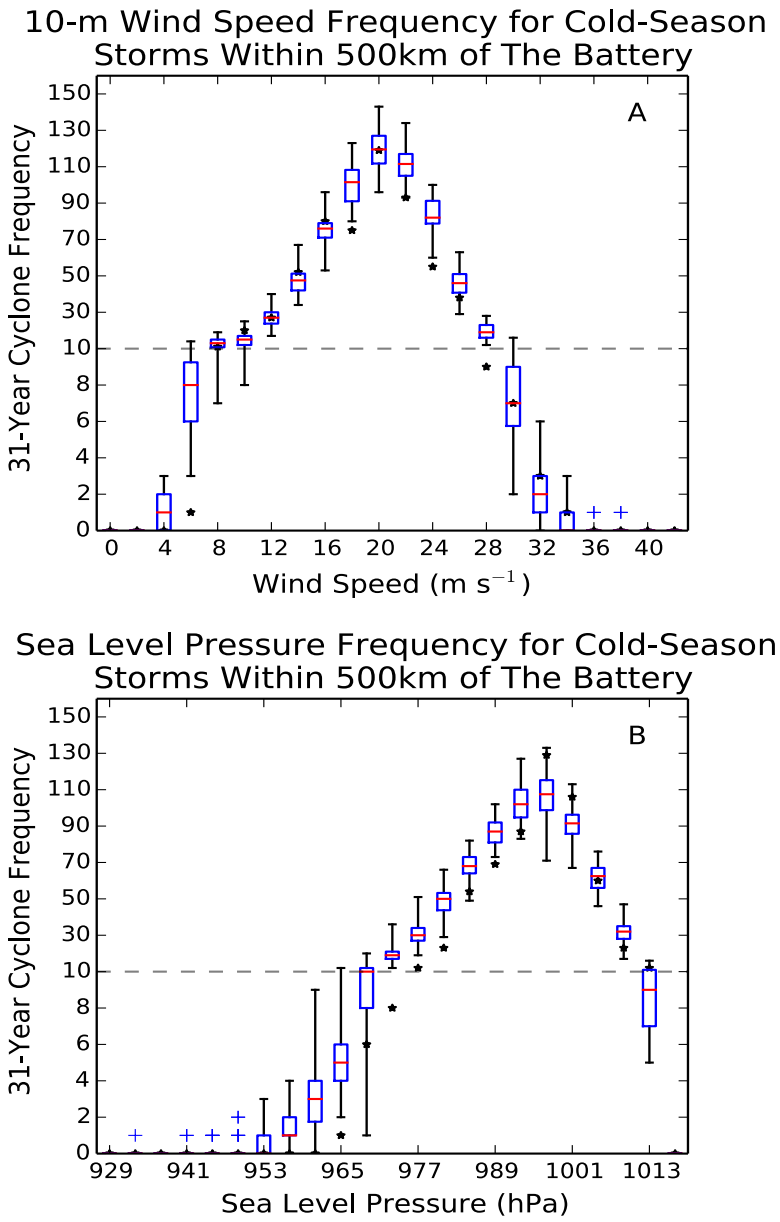

Fig. 3.7. Box-and-whisker plots of (a) maximum 10-m wind speed values (in m s^{-1}) and (b) minimum SLP values (in hPa) within 500 km of The Battery for cold-season storms across FLOR 31-year subsamples. Black asterisks indicate CFSR values. The top and bottom of the boxes represent the 75th and 25th percentiles, respectively, and red lines within each box indicate the median value. Whiskers span the range of data (minimum to maximum). Note: frequency intervals differ below the dashed line to magnify lower frequency behavior.

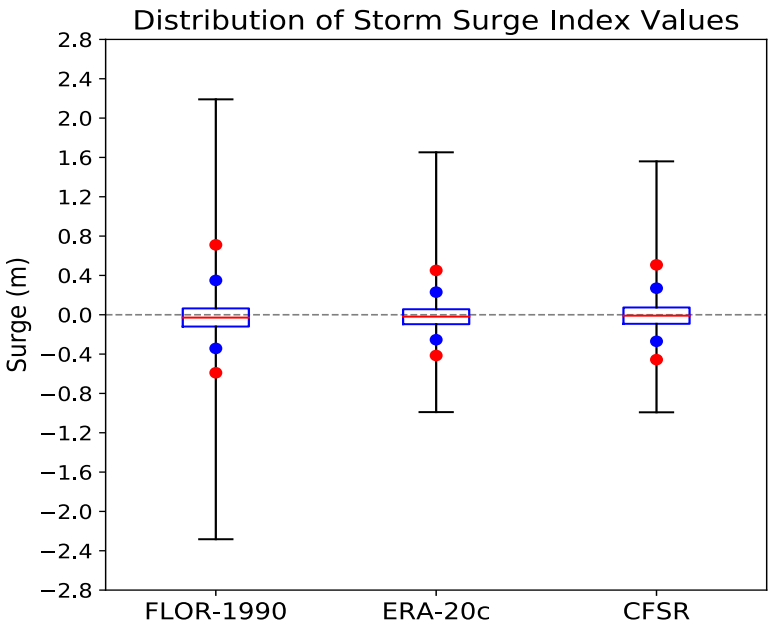

Fig. 3.8. Box-and-whisker plots of storm surge indices (in m) for all 6-hourly data from FLOR, ERA20c, and CFSR. The top and bottom of the boxes represent the 75th and 25th percentiles, respectively, and red lines within each box indicate the median value. Blue circles indicate 5th and 95th percentiles, and red circles specify surge values at 1st and 99th percentiles. Whiskers span the range of data (minimum to maximum).

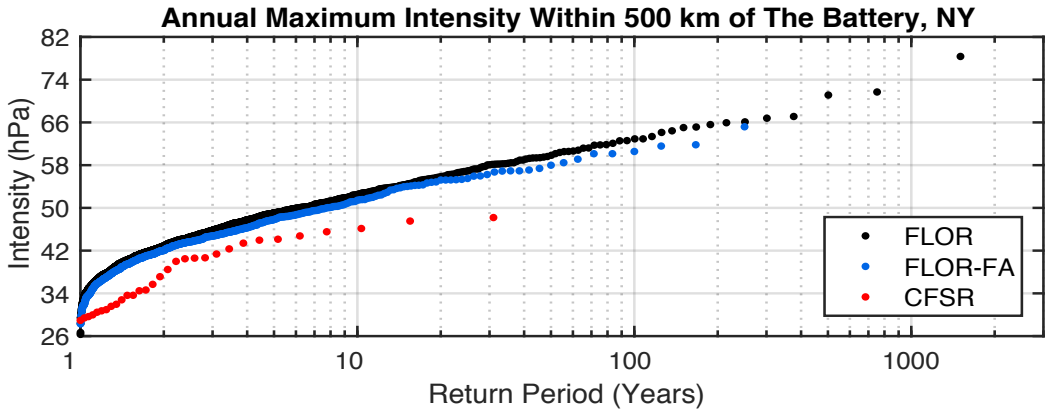

Fig. 3.9. Maximum annual cold-season intensity values (in hPa) within 500 km of The Battery as a function of return period for FLOR (black), FLOR-FA (blue) and CFSR (red). Rightmost points indicate the lengths of the records.

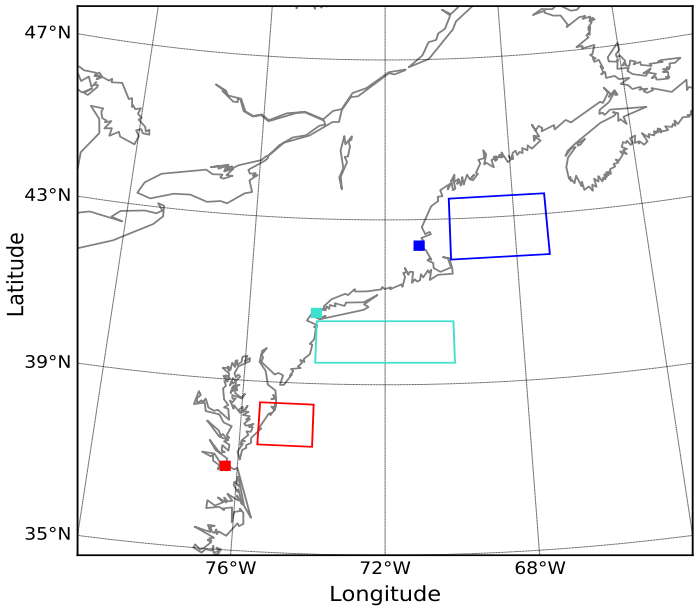

Fig. 4.1. Regions over which the storm surge index is applied at Boston, Massachusetts (blue); The Battery, New York (turquoise); and Sewells Point, Virginia (red). Locations are identified by filled circles in corresponding colors.

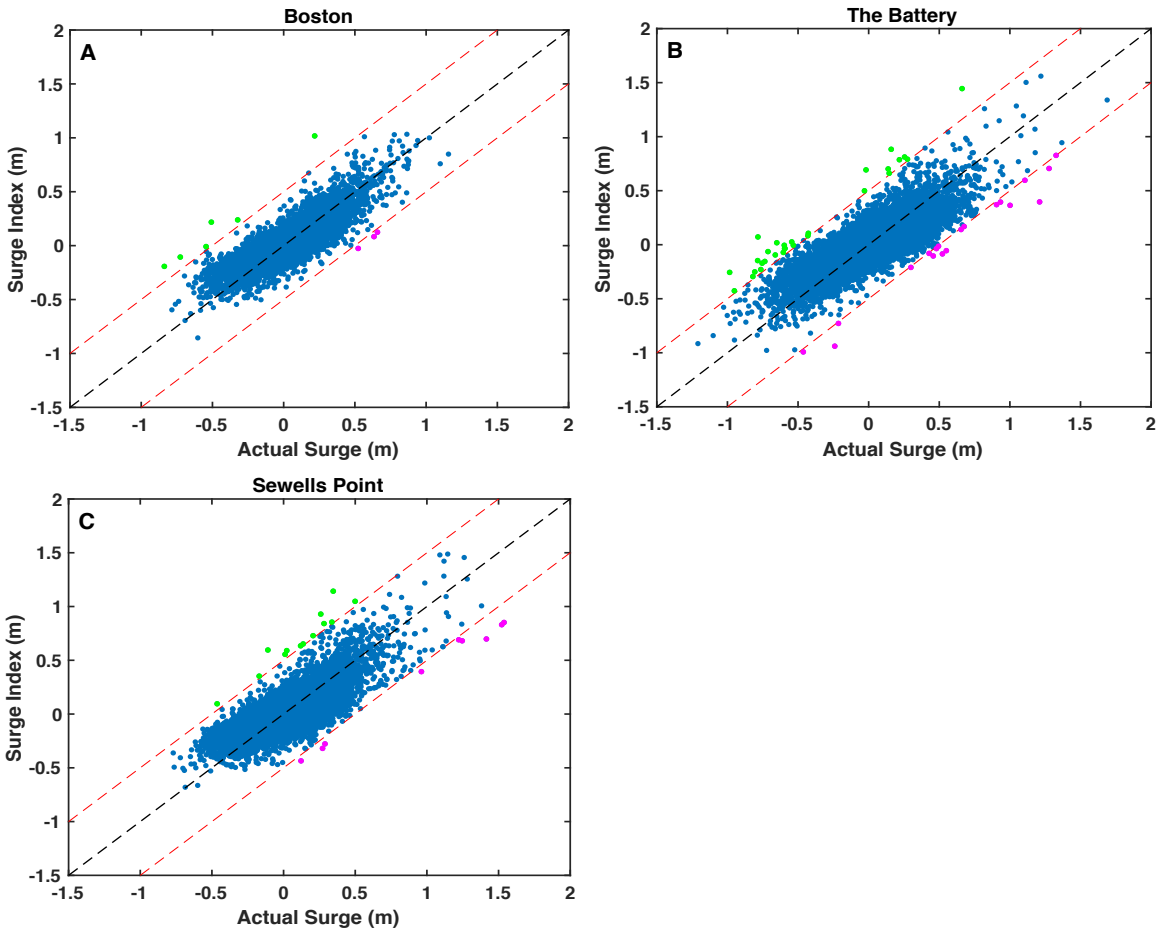

Fig. 4.2. Scatterplots of observed storm surge and CFSR surge index values (m) during the cold season (November–April) at Boston, The Battery, and Sewells Point (1979–2009). The dashed black line represents a 1:1 ratio, and dashed red lines are residuals ± 0.5 m as a measure of uncertainty. Green circles highlight surge values that are overestimated by the index, whereas magenta circles indicate underestimated values.

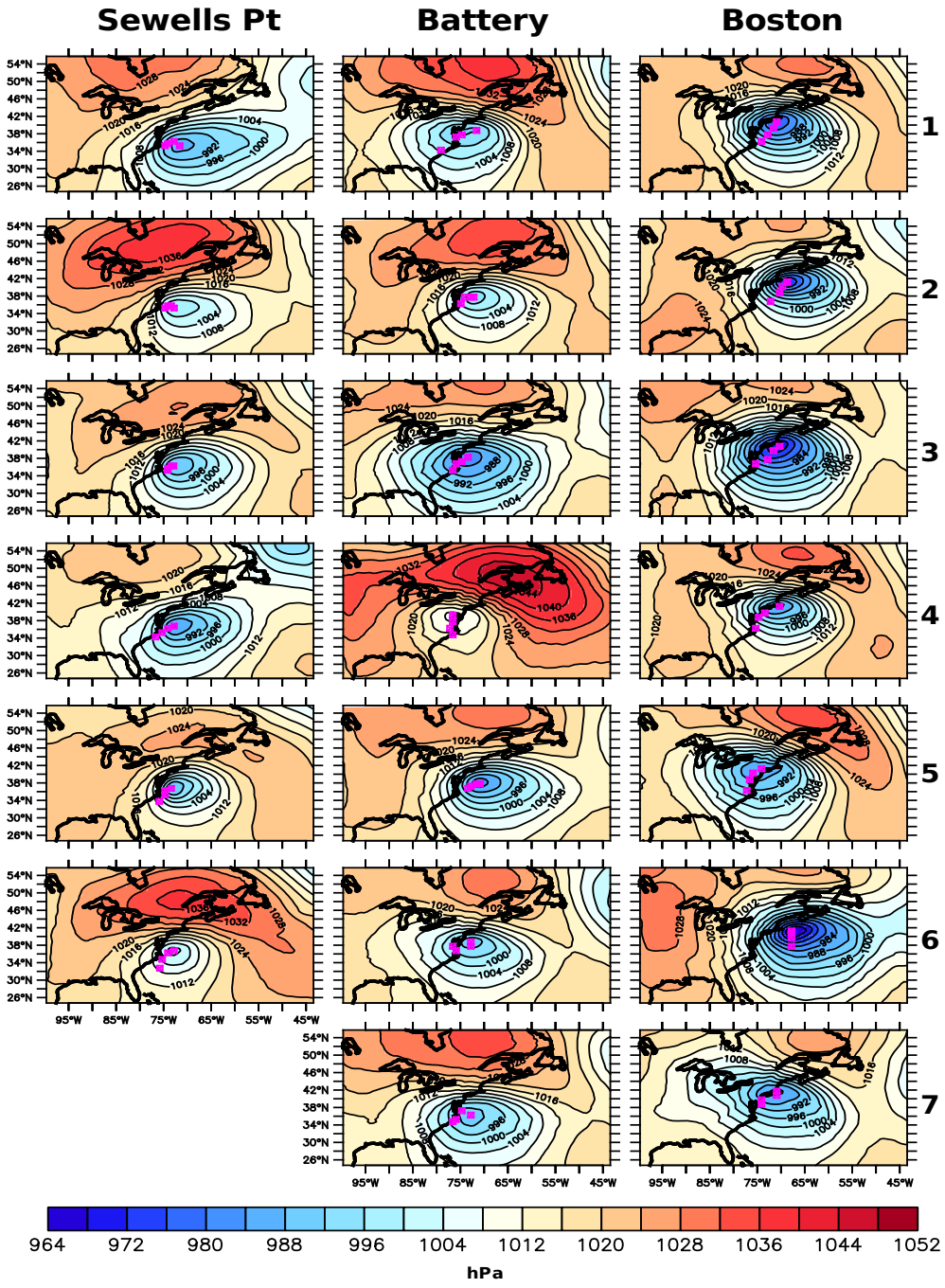

Fig. 4.3. Cluster centroids (numbered top to bottom) for 100 largest SSI events at Sewells Point, The Battery, and Boston organized by decreasing associated surge values. Each map depicts the cluster centroid at time before maximum surge ($t = 0$). Average cyclone centers at 0-, 6-, 12-, and 18- hour lags ($t = 0$, $t = -6$, $t = -12$, $t = -18$) are marked in magenta.

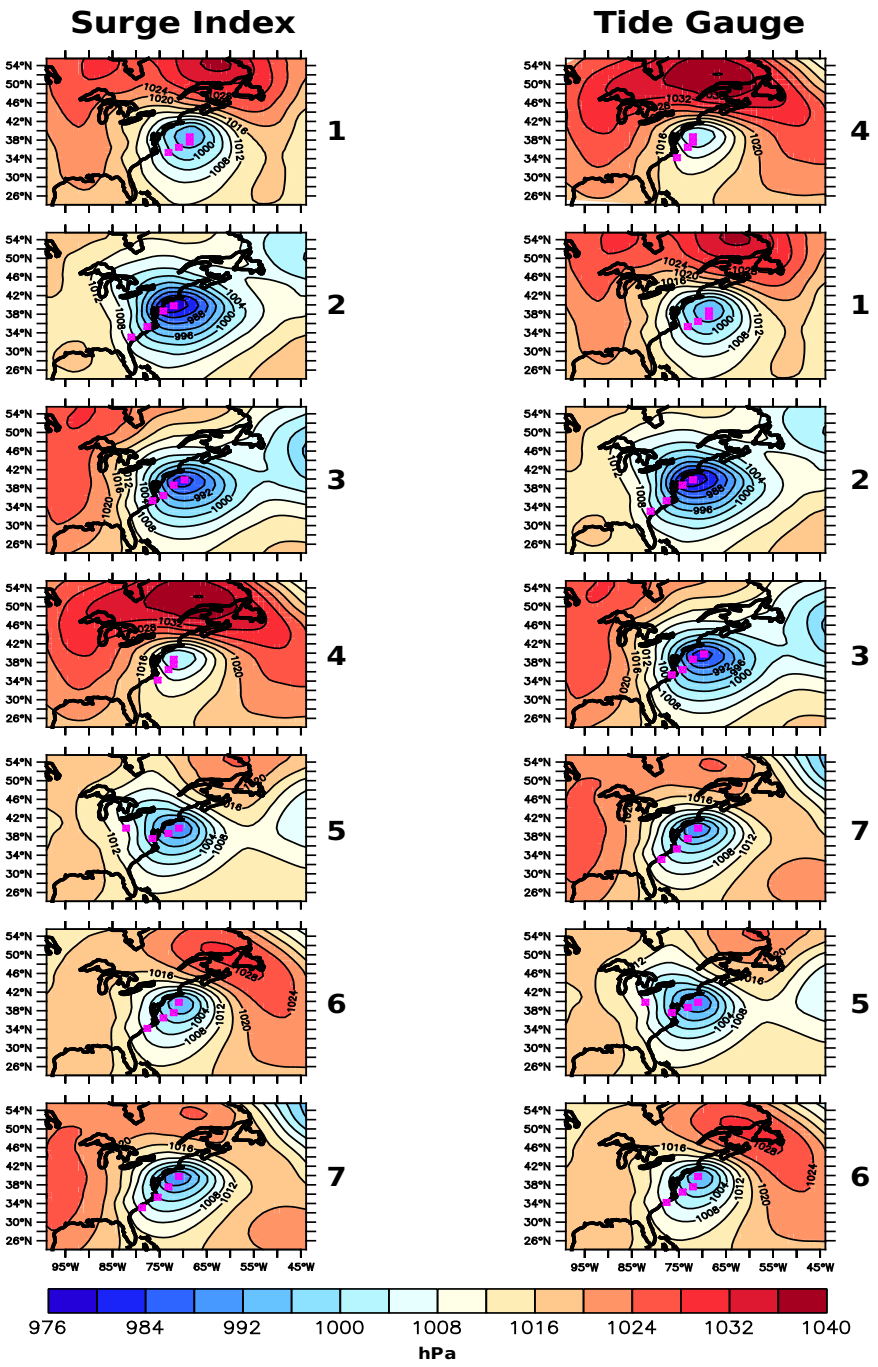

Fig. 4.4. As in Fig. 4.3, but for clustered SLP fields (in hPa) from ERA20c associated with the 100 largest SSI events at Boston (1921–2010). Centroids in the left column are organized by decreasing SSI values (numbered), whereas centroids in the right column are organized by decreasing observed surge levels for related events. Numbers in the right column correspond to numbered clusters from the left column.

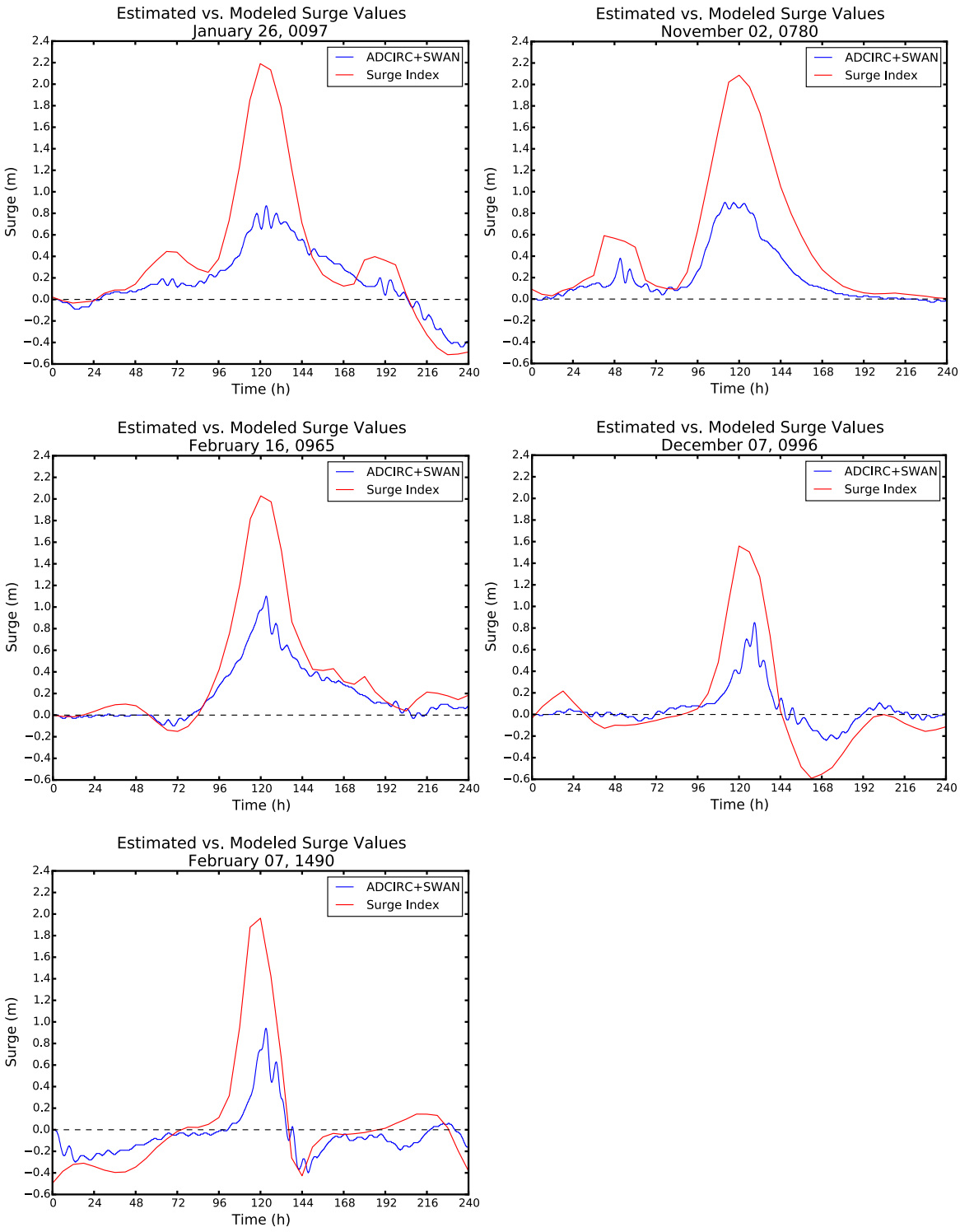

Fig. 4.5. Simulated surge levels from ADCIRC+SWAN (blue) and estimated surge values from the storm surge index (red) for five select events in FLOR. The dashed line separates positive and negative surge values.

References

Athanasiadis, P. J., J. M. Wallace, and J. J. Wettstein, 2010: Patterns of wintertime jet stream variability and their relation to the storm tracks. *J. Atmos. Sci.*, **67**, 1361–1381, https://doi.org/10.1175/2009JAS3270.1.

Bengtsson, L., K. I. Hodges, and N. Keenlyside, 2009: Will extratropical storms intensify in a warmer climate? *J. Climate*, **22**, 2276–2301, https://doi.org/10.1175/2008JCLI2678.1.

Bernhardt, J. E., and A. T. DeGaetano, 2012: Meteorological factors affecting the speed of movement and related impacts of extratropical cyclones along the U.S. East Coast. *Nat. Hazards*, **61**, 1463–1472, https://doi.org/10.1007/s11069-011-0078-0.

Blender, R., K. Fraedrich, and F. Lunkeit, 1997: Identification of cyclone-track regimes in the North Atlantic. *Quart. J. Roy. Meteor. Soc*., **123**, 727–741, https://doi.org/10.1002/qj.49712353910.

Booij, N., Ris, R. C., and Holthuijsen, L. H., 1999: A third-generation wave model for coastal regions. 1: Model description and validation. *J. of Geophys. Res,*, **104**(C4), 7649–7666, https://doi.org/10.1029/98JC02622.

Booth, J. F., C. Naud, and A. D. Del Genio, 2013: Diagnosing warm frontal cloud formation in a GCM: A novel approach using conditional subsetting. *J. Climate*, **26**, 5827–5845, https://doi.org/10.1175/JCLI-D-12-00637.1.

____, H. E. Rieder, D. E. Lee, and Y. Kushnir, 2015: The paths of extratropical cyclones associated with wintertime high-wind events in the northeastern United States. *J. Appl. Meteor. Climatol*., **54**, 1871–1885, https://doi.org/10.1175/JAMC-D-14-0320.1.

——, H. E. Rieder, and Y. Kushnir, 2016: Comparing hurricane and extratropical storm surge for the mid-Atlantic and northeast coast of the United States for 1979–2013. *Environ. Res. Lett.*,**11**, 094004, https://doi.org/10.1088/1748-9326/11/9/094004.

Burlando, M., 2009: The synoptic-scale surface wind climate regimes of the Mediterranean Sea according to the cluster analysis of ERA-40 wind fields. *Theor. Appl. Climatol*., **96**, 69–83, https://doi.org/10.1007/s00704-008-0033-5.

Catalano, A. J., and A. J. Broccoli, 2018: Synoptic characteristics of surge-producing extratropical cyclones along the Northeast Coast of the United States. *J. Appl. Meteor. Climatol.*, **57**, 171–184.

Catto, J. L., L. C. Shaffrey, and K. I. Hodges, 2011: Northern Hemisphere extratropical

cyclones in a warming climate in the HiGEM high-resolution climate model. *J. Climate,* **24**, 5336–5352, https://doi.org/10.1175/2011JCLI4181.1.

Chen, D., M. A. Cane, A. Kaplan, S. E. Zebiak, and D. Huang, 2004: Predictability of El Niño over the past 148 years. *Nature*, **428**, 733–736, https://doi.org/10.1038/nature02439.

Clifton, A., and J. K. Lundquist, 2012: Data clustering reveals climate impacts on local wind phenomena. *J. Appl. Meteor. Climatol*., **51**, 1547–1557, https://doi.org/10.1175/JAMC-D-11-0227.1.

Coles, S., 2001: An Introduction to Statistical Modeling of Extreme Values (London: Springer).

Colle, B. A., F. Buonaiuto, M. J. Bowman, R. E. Wilson, R. Flood, R. Hunter, A. Mintz, and D. Hill, 2008: New York City's vulnerability to coastal flooding*, Bull. Amer. Meteorol. Soc.*, **89**, 829–841, doi:10.1175/2007BAMS2401.1.

____, K. Rojowsky, and F. Buonaito, 2010: New York City storm surges: Climatology and an analysis of the wind and cyclone evolution. *J. Appl. Meteor. Climatol*., **49**, 85–100, https://doi.org/10.1175/2009JAMC2189.1.

——, Z. Zhang, K. A. Lombardo, E. Chang, P. Liu, and M. Zhang, 2013: Historical evaluation and future prediction of eastern North American and western Atlantic extratropical cyclones in the CMIP5 models during the cool season. *J. Climate*, **26**, 6882–6903, https://doi.org/10.1175/JCLI-D-12-00498.1.

Delworth, T. L., A. J. Broccoli, A. Rosati, R. J. Stouffer, V. Balaji, J. A. Beesley, W. F. Cooke, K. W. Dixon, J. Dunne, K. A. Dunne, J. W. Durachta, K. L. Findell, P. Ginoux, A. Gnanadesikan, C. T. Gordon, S. M. Griffies, R. Gudgel, M. J. Harrison, I. M. Held, R. S. Hemler, L. W. Horowitz, S. A. Klein, T. R. Knutson, P. J. Kushner, A. R. Langenhorst, H. Lee, S. Lin, J. Lu, S. L. Malyshev, P. C. Milly, V. Ramaswamy, J. Russell, M. D. Schwarzkopf, E. Shevliakova, J. J. Sirutis, M. J. Spelman, W. F. Stern, M. Winton, A. T. Wittenberg, B. Wyman, F. Zeng, and R. Zhang, 2006: GFDL's CM2 global coupled climate models. Part 1: formulation and simulation characteristics. *J. Climate*, **19**, 643–674, https://doi.org/10.1175/JCLI3629.1.

——, A. Rosati, W. Anderson, A. J. Adcroft, V. Balaji, R. Benson, K. Dixon, S. M. Griffies, H. Lee, R. C. Pacanowski, G. A. Vecchi, A. T. Wittenberg, F. Zeng, and R. Zhang, 2012: Simulated climate and climate change in the GFDL CM2.5 high-resolution coupled climate model. *J. Climate*, **25**, 2755–2781, https://doi.org/10.1175/JCLI-D-11-00316.1.

Dietrich, J. C., M. Zijlema, J. J. Westerink, L. H. Holthuijsen, C. Dawson, R. A. Luettich, R. E. Jensen, J. M. Smith, G. S. Stelling, and G. W. Stone 2011: Modeling hurricane waves and storm surge using integrally-coupled, scalable computations.

Coast. Eng., **58**, 45–65.

____, Tanaka, S., Westerink, J. J., C. N. Dawson, R. A. Luettich Jr., M. Zijlema, L. H. Holthuijsen, J. M. Smith, L. G. Westerink, H. J. Westerink, 2012: Performance of the unstructured-mesh, SWAN+ADCIRC model in computing hurricane waves and surge. *J. Sci. Comput.,* **52,** 468–497, https://doi.org/10.1007/s10915-011-9555-6.

Eichler, T., and W. Higgins, 2006: Climatology and ENSO related variability of North American extratropical cyclone activity. *J. Climate,* **19**, 2076–2093, https://doi.org/10.1175/JCLI3725.1.

Emanuel, K., S. Ravela, E. Vivant, and C. Risi, 2006: A statistical deterministic approach of hurricane risk assessment. *Bull. Amer. Meteor. Soc.*, **87**, 299–314.

Feldstein, S. B., 2000: The timescale, power spectra, and climate noise properties of teleconnection patterns. *J. Climate,* **13**, 4430–4440, https://doi.org/10.1175/1520-0442(2000)013,4430:TTPSAC.2.0.CO;2.

Grise, K. M., S.-W. Son, and J. R. Gyakum, 2013: Intraseasonal and interannual variability in North American storm tracks and its relationship to equatorial Pacific variability. *Mon. Wea. Rev*., **141**, 3610–3625, https://doi.org/10.1175/MWR-D-12-00322.1.

Gulev, S. K., O. Zolina, and S. Grigoriev, 2001: Extratropical cyclone variability in the Northern Hemisphere winter from the NCEP/NCAR reanalysis data. *Climate Dyn.,* **17**, 795–809, https://doi.org/10.1007/s003820000145.

Hall, T. and E. Yonekura, 2013: North American tropical cyclone landfall and SST: A statistical model study. *J. Climate*, **26**, 8422–8439.

——, and J. F. Booth, 2017: SynthETC: A statistical model for severe winter storm hazard on eastern North America. *J. Climate*, **30**, 5329–5343, https://doi.org/10.1175/JCLI-D-16-0711.1.

Hodges, K. I., B. J. Hoskins, J. Boyle, and C. Thorncroft, 2003: A comparison of recent reanalysis datasets using objective feature tracking: Storm tracks and tropical easterly waves. *Mon. Wea. Rev,*, **131**, 2012–2037, https://doi.org/10.1175/1520-0493(2003)131<2012:ACORRD>2.0.CO;2.

——, R. W. Lee, and L. Bengtsson, 2011: A comparison of extratropical cyclones in recent reanalyses ERA-Interim, NASA MERRA, NCEP CFSR, and JRA-25. *J. Climate*, **24**, 4888–4906, https://doi.org/10.1175/2011JCLI4097.1.

Hope, M. E., J. J. Westerink, A. B. Kennedy, P. C. Kerr, J. C. Dietrich, C. Dawson, C. J. Bender, J. M. Smith, R. E. Jensen, M. Zijlema, L. H. Holthuijsen, R. A. Luettich Jr., M. D. Powell, V. J. Cardone, A. T. Cox, H. Pourtaheri, H. J. Roberts, J. H. Atkinson,

S. Tanaka, H. J. Westerink, and L. G. Westerink, 2013: Hindcast and validation of Hurricane Ike (2008) waves, forerunner, and storm surge. *J. Geophys. Res. Oceans*, **118**, 4424–4460, https://doi.org/10.1002/jgrc.20314.

Hoskins, B. J., and K. I. Hodges, 2002: New perspectives on the Northern Hemisphere winter storm tracks. *J. Atmos. Sci.*, **59**, 1041–1061.

Jia, L., X. Yang, G. A. Vecchi, R. G. Gudgel, T. L. Delworth, A. Rosati, W. F. Stern, A. T. Wittenberg, L. Krishnamurthy, S. Zhang, R. Msadek, S. Kapnick, S. Underwood, F. Zeng, W. G. Anderson, V. Balaji, and K. Dixon, 2015: Improved seasonal prediction of temperature and precipitation over land in a high-resolution GFDL climate model. *J. Climate*, **28**, 2044–2062, http://dx.doi.org/10.1175/JCLI-D-14-00112.1.

Kaufman, L., and P. J. Rousseeuw, 1990: Finding Groups in Data: An Introduction to Cluster Analysis. John Wiley and Sons, 342 pp.

Kocin, P., P. Schumacher, R. Morales, and L. Uccellini, 1995. Overview of the 12-14 March 1993 Superstorm. *Bull. Amer. Meteor. Soc.*, **76**, 2, 165–182.

Leckebusch, G. C., A. Weimer, J. G. Pinto, M. Reyers, and P. Speth, 2008: Extreme wind storms over Europe in present and future climate: A cluster analysis approach. *Meteor. Z.*, **17**, 67–82, https://doi.org/10.1127/0941-2948/2008/0266.

Lin, N., K. A. Emanuel, J. A. Smith, and E. Vanmarcke, 2010: Risk assessment of hurricane storm surge for New York City, *J. Geophys. Res.*, **115**, D18121, doi:10.1029/2009JD013630.

____, ____, M. Oppenheimer, and E. Vanmarcke, 2012: Physically based assessment of hurricane surge threat under climate change. *Nat. Climate Change*, **2**, 462–467, https://doi.org/10.1038/nclimate1389.

____, ____, 2016: Grey swan tropical cyclones. *Nat. Clim. Change,* **6**, 106–111, http://dx.doi.org/10.1038/nclimate2777.

Luettich R.A., J. J. Westerink, and N. W. Scheffner, 1992: ADCIRC: An Advanced Three dimensional Circulation Model for Shelves, Coasts and Estuaries, Report 1: Theory and Methodology of ADCIRC-2DDI and ADCIRC-3DL. DRP Technical Report DRP-92-6. (Department of the Army, US Army Corps of Engineers, Waterways Experiment Station, Vicksburg, MS, 1992).

MacQueen, J., 1967: Some methods for classification and analysis of multivariate observations. Proceedings of the Fifth Berkeley Symposium on Mathematical Statistics and Probability, Vol. 1, University of California Press, 281–297, http://projecteuclid.org/euclid.bsmsp/1200512992.

Marsooli, R., and N. Lin, 2018: Numerical modeling of historical storm tides and waves

and their interactions along the U.S. east and Gulf Coasts. *J. of Geophys. Res.*: *Oceans*, **123**, https://doi.org/10.1029/2017JC013434.

Michelangeli, P.-A., R. Vautard, and B. Legras, 1995: Weather regimes: Recurrence and quasi-stationarity. *J. Atmos. Sci*., **52**, 1237–1256, https://doi.org/10.1175/1520-0469(1995)052,1237:WRRAQS.2.0.CO;2.

Munroe, R., and S. Curtis, 2017: Storm surge evolution and its relationship to climate oscillations at Duck, NC. *Theor. Appl. Climatol.,* **129**, 185–200, https://doi.org/10.1007/s00704-016-1770-5.

Orton, P. M., T. M. Hall, S. A. Talke, A. F. Blumberg, N. Georgas, and S. Vinogradov, 2016: A validated tropical-extratropical flood hazard assessment for New York harbor. *J. Geophys. Res. Oceans*, **121**, 8904–8929, https://doi.org/10.1002/2016JC011679.

Poli, P., H. Hersbach, D. P. Dee, P. Berrisford, A. J. Simmons, F. Vitart, P. Laloyaux, D. G. H. Tan, C. Peubey, J.-N. Thépaut, Y. Trémolet, E. V. Hólm, M. Bonavita, L. Isaksen, and M. Fisher, 2016: ERA-20C: An atmospheric reanalysis of the twentieth century. *J. Climate*, **29**, 4083–4097, https://doi.org/10.1175/JCLI-D-15-0556.1.

Raible, C. C., P. M. Della-Marta, C. Schwierz, H. Wernli, and R. Blender, 2008: Northern Hemisphere extratropical cyclones: A comparison of detection and tracking methods and different reanalyses. *Mon. Wea. Rev*., **136**, 880–897, https://doi.org/10.1175/2007MWR2143.1.

Reed, A. J., M. E. Mann, K. A. Emanuel, N. Lin, B. P. Horton, A. C. Kemp, and J. P. Donnelly, 2015: Increased threat of tropical cyclones and coastal flooding to New York City during the anthropogenic era. *Proc. Natl Acad. Sci.* **112**, 12610–12615.

Rex, D. F., 1950: Blocking action in the middle troposphere and its effect upon regional climate. *Tellus*, **2,** 275–301, doi:10.1111/j.2153-3490.1950.tb00339.x.

Ris, R. C., Holthuijsen, L. H., and Booij, N., 1999: A third-generation wave model for coastal regions: 2. Verification. *J. of Geophys. Res.*, **104**(C4), 7649–7666, https://doi.org/10.1029/1998JC900123.

Roberts, K. J., B. A. Colle, N. Georgas, and S. B. Munch, 2015: A regression-based approach for cool-season storm surge predictions along the New York–New Jersey coast. *J. Appl. Meteor. Climatol.,* **54,** 1773–1791, https://doi.org/10.1175/JAMC-D-14-0314.1.

——, ——, and N. Korfe, 2017: Impact of simulated twenty-first-century changes in extratropical cyclones on coastal flooding at The Battery, New York City. *J. Appl. Meteor. Climatol.,* **56**, 415–432, https://doi.org/10.1175/JAMC-D-16-0088.1.

Saha, S., S. Moorthi, H. Pan, X. Wu, J. Wang, S. Nadiga, P. Tripp, R. Kistler, J. Woollen, D. Behringer, H. Liu, D. Stokes, R. Grumbine, G. Gayno, J. Wang, Y. Hou, H. Chuang, H.H. Juang, J. Sela, M. Iredell, R. Treadon, D. Kleist, P. Van Delst, D. Keyser, J. Derber, M. Ek, J. Meng, H. Wei, R. Yang, S. Lord, H. Van Den Dool, A. Kumar, W. Wang, C. Long, M. Chelliah, Y. Xue, B. Huang, J. Schemm, W. Ebisuzaki, R. Lin, P. Xie, M. Chen, S. Zhou, W. Higgins, C. Zou, Q. Liu, Y. Chen, Y. Han, L. Cucurull, R.W. Reynolds, G. Rutledge, and M. Goldberg, 2010: The NCEP Climate Forecast System Reanalysis. *Bull. Amer. Meteor. Soc.*, **91**, 1015–1057, http://dx.doi.org/10.1175/2010BAMS3001.1.

Shabbar, A., J. Huang, and K. Higuchi, 2001: The relationship between the wintertime North Atlantic Oscillation and blocking episodes in the North Atlantic. *Int. J. Climatol.,* **21**, 355–369, https://doi.org/10.1002/joc.612.

Smith, C. D., Jr., 1950: The destructive storm of November 25–27, 1950. *Mon. Wea. Rev*., **78**, 204–209, https://doi.org/10.1175/1520-0493(1950)078,0204:TDSON.2.0.CO;2.

Stopa, J. E., and K. F. Cheung, 2014: Intercomparison of wind and wave data from the ECMWF Reanalysis Interim and the NCEP Climate Forecast System Reanalysis. *Ocean Modell.*, **75**, 65–83, https://doi.org/10.1016/j.ocemod.2013.12.006.

Sweet, W. V., and C. Zervas, 2011: Cool-season sea level anomalies and storm surges along the U.S. East Coast: Climatology and comparison with the 2009/10 El Niño. *Mon. Wea. Rev.*, **139**, 2290–2299, https://doi.org/10.1175/MWR-D-10-05043.1.

——, ——, S. Gill, and J. Park, 2013: Hurricane Sandy inundation probabilities today and tomorrow [in ‘‘Explaining Extreme Events of 2012 from a Climate Perspective’’]. *Bull. Amer. Meteor. Soc.*, **94**(9), S17–S20.

Talke, S. A., P. Orton, and D. A. Jay, 2014: Increasing storm tides in New York harbor, 1844–2013. *Geophys. Res. Lett.,* **41**, 3149–3155, https://doi.org/10.1002/2014GL059574.

Teng, H., W. M. Washington, and G. A. Meehl, 2008: Interannual variations and future change of wintertime extratropical cyclone activity over North America in CCSM3. *Climate Dyn.,* **30**, 673–686, https://doi.org/10.1007/s00382-007-0314-1.

Thompson, D. W. J., and J. M. Wallace, 2001: Regional climate impacts of the Northern Hemisphere annular mode. *Science*, **293**, 85–89, https://doi.org/10.1126/science.1058958.

Trenberth, K. E., and D. P. Stepaniak, 2001: Indices of El Niño evolution. *J. Climate*, **14**, 1697–1701, https://doi.org/10.1175/1520-0442(2001)014,1697:LIOENO.2.0.CO;2.

USACE, 2015: *North Atlantic Coast Comprehensive Study: Resilient Adaptation to Increasing Risk: Main Report*, 140 pp., U.S. Army Corps of Eng.

van der Wiel, K., Kapnick, S. B., Oldenborgh, G. J. V., Whan, K., Philip, S., Vecchi, G. A., Singh, R. K., Arrighi, J. and H. Cullen, 2017: Rapid attribution of the August 2016 flood-inducing extreme precipitation in south Louisiana to climate change. *Hydrology and Earth System Sciences*, **21**, 897–921.

van der Wiel, K., Kapnick, S. B., Vecchi, G. A., Smith, J. A., Milly, P. C. D., and L. Jia, 2018: 100-yr Lower Mississippi floods in a global climate model: characteristics and future changes. *In Revision, J. of Hydrometeorology.*

Vecchi, G. A., T. Delworth, R. Gudgel, S. Kapnick, A. Rosati, A. T. Wittenberg, F. Zeng, W. Anderson, V. Balaji, K. Dixon, L. Jia, H. Kim, L. Krishnamurthy, R. Msadek, W. F. Stern, S. D. Underwood, G. Villarini, X. Yang, and S. Zhang, 2014: On the Seasonal Forecasting of Regional Tropical Cyclone Activity. *J. Climate*, **27**, 7994–8016, https://doi.org/10.1175/JCLI-D-14-00158.1.

Westerink, J. J., R. A. Luettich, C. A. Blain, and N. W. Scheffner, 1994: ADCIRC: An advanced three-dimensional circulation model for shelves, coasts, and estuaries. Report 2: User's Manual for ADCIRC-2DDI, Dredging Research Program Tech. Rep. DRP-92-6, Coastal Eng. Res. Cent., Vicksburg, Miss.

Whitfield, P. H., A. W. Hall, and A. J. Cannon, 2004: Changes in the seasonal cycle in the circumpolar Arctic, 1976–95: Temperature and precipitation. *Arctic*, **57**, 80–93, https://doi.org/10.14430/arctic485.

Xia, L., H. von Storch, and F. Feser, 2013: Quasi-stationarity of centennial Northern Hemisphere midlatitude winter storm tracks. *Climate Dyn.,* **41**, 901–916, https://doi.org/10.1007/s00382-012-1543-5.

Yang, X., G. A. Vecchi, R. G. Gudgel, T. L. Delworth, S. Zhang, A. Rosati, L. Jia, W. F. Stern, A. T. Wittenberg, S. Kapnick, R. Msadek, S.D. Underwood, F. Zeng, W. Anderson, and V. Balaji, 2015: Seasonal predictability of extratropical storm tracks in GFDL's high-resolution climate prediction model. *J. Climate*, **28**, 3592–3611, https://doi.org/10.1175/JCLI-D-14-00517.1.

Zhang, K., B. C. Douglas, and S. P. Leatherman, 2000: Twentieth century storm activity along the U.S. East Coast. *J. Climate*, **13**, 1748–1761, https://doi.org/10.1175/1520-0442(2000)013,1748:TCSAAT.2.0.CO;2.

Zhang, W., G. A. Vecchi, G. Villarini, H. Murakami, R. Gudgel, and X. Yang, 2017: Statistical–dynamical seasonal forecast of western North Pacific and East Asia landfalling tropical cyclones using the GFDL FLOR coupled climate model. *J. Climate*, **30**, 2209–2232, https://doi.org/10.1175/JCLI-D-16-0487.1.

Zhao, M., I. M. Held, S.-J. Lin, and G. A. Vecchi, 2009: Simulations of global hurricane climatology, interannual variability, and response to global warming using a 50-km resolution GCM. *J. Climate*, **22**, 6653–6678, https://doi.org/10.1175/2009JCLI3049.1.